

LyC escape from SPHINX galaxies in the Epoch of Reionization

Joakim Rosdahl¹*, J r my Blaizot¹, Harley Katz², Taysun Kimm³, Thibault Garel⁴,
Martin Haehnelt⁵, Laura C. Keating⁶, Sergio Martin-Alvarez⁵, L o Michel-Dansac¹,
and Pierre Ocvirk⁷

¹Univ Lyon, Univ Lyon1, Ens de Lyon, CNRS, Centre de Recherche Astrophysique de Lyon UMR5574, F-69230, Saint-Genis-Laval, France

²Sub-department of Astrophysics, University of Oxford, Keble Road, Oxford OX1 3RH, UK

³Department of Astronomy, Yonsei University, 50 Yonsei-ro, Seodaemun-gu, Seoul 03722, Republic of Korea

⁴Observatoire de Gen ve, Universit  de Gen ve, 51 Ch. des Maillettes, 1290 Versoix, Switzerland

⁵Kavli Institute for Cosmology and Institute of Astronomy, Madingley Road, Cambridge CB3 0HA, UK

⁶Leibniz-Institute for Astrophysics Potsdam (AIP), An der Sternwarte 16, 14482 Potsdam, Germany

⁷Observatoire Astronomique de Strasbourg, Universit  de Strasbourg, CNRS UMR 7550, 11 rue de l'Universit , 67000 Strasbourg, France

Accepted XXX. Received YYY; in original form ZZZ

ABSTRACT

We measure escape fractions, f_{esc} , of ionizing radiation from galaxies in the SPHINX suite of cosmological radiation-hydrodynamical simulations of reionization, resolving halos with $M_{\text{vir}} \gtrsim 7.5 \times 10^7 M_{\odot}$ with a minimum cell width of ≈ 10 pc. Our new and largest 20 co-moving Mpc wide volume contains tens of thousands of star-forming galaxies with halo masses up to a few times $10^{11} M_{\odot}$. The simulated galaxies agree well with observational constraints of the UV luminosity function in the Epoch of Reionization. The escape fraction fluctuates strongly in individual galaxies over timescales of a few Myrs, due to its regulation by supernova and radiation feedback, and at any given time a tiny fraction of star-forming galaxies emits a large fraction of the ionizing radiation escaping into the inter-galactic medium. Statistically, f_{esc} peaks in intermediate-mass, intermediate-brightness, and low-metallicity galaxies ($M_{*} \approx 10^7 M_{\odot}$, $M_{1500} \approx -17$, $Z \lesssim 5 \times 10^{-3} Z_{\odot}$), dropping strongly for lower and higher masses, brighter and dimmer galaxies, and more metal-rich galaxies. The escape fraction correlates positively with both the short-term and long-term specific star formation rate. According to SPHINX, galaxies too dim to be yet observed, with $M_{1500} \gtrsim -17$, provide about 55 percent of the photons contributing to reionization. The global averaged f_{esc} naturally decreases with decreasing redshift, as predicted by UV background models and low-redshift observations. This evolution is driven by decreasing specific star formation rates over cosmic time.

Key words: early Universe – dark ages, reionization, first stars – galaxies: high-redshift – methods: numerical

1 INTRODUCTION

Following the Big Bang, the Universe underwent rapid expansion and cooling. When reaching a temperature of a few thousand Kelvin, protons and electrons recombined, forming atoms. The moment of this transition from an ionized to neutral Universe is perpetually observable in the Cosmic Microwave Background (CMB; Penzias & Wilson 1965). However these neutral Dark Ages did not last forever: about a billion years later, the reverse transition took place and the inter-galactic medium (IGM) became reionized, a state in which it remains today.

There is much still to be understood about reionization. Observationally it is known from the Thomson optical depth for CMB radiation (e.g. Planck Collaboration et al. 2018), the Gunn-Peterson trough (Gunn et al. 1965), and observations of extreme-redshift Lyman-alpha emitters (e.g. Inoue et al. 2018), that the Epoch of Reionization (EoR) lasted for several hundred million years and most likely ended between redshifts 6 and 5 (Keating et al. 2020; Becker et al. 2021).

It is commonly assumed that reionization was driven by ionizing Lyman-continuum (LyC) radiation from massive stars in the first galaxies. In this scenario, the redshift-evolution of the ionized hydrogen fraction in the IGM can be modelled with four parameters that describe the competition between star-powered photo-ionization and recombination of atoms (Madau et al. 1999): for photo-ionization i) the star formation rate density (SFRD) in the early Universe, ii) the number of LyC photons produced per unit stellar mass formed, and iii) the fraction – f_{esc} – of the LyC photons produced by stars that make it out of the inter-stellar medium (ISM) of their source galaxies and into the IGM – and for recombination iv) the clumping factor of the IGM which sets the average recombination rate. Out of those four parameters, the escape fraction of LyC photons from galaxies is the most poorly understood.

Observationally, direct measurements of f_{esc} are not feasible at $z \gtrsim 4$ because almost all the LyC radiation is absorbed by the intervening IGM on its way to the observer (Inoue & Iwata 2008). Indirect measurements are made using metal-line ratios, but these ratios are still not well understood (Katz et al. 2020b, 2021) and hence the derived escape fractions are poorly constrained. At lower redshift direct and indirect measurements can be made of escape fractions

* E-mail: karl-joakim.rosdahl@univ-lyon1.fr

from individual galaxies but these are difficult and highly uncertain and they tend to vary a lot both from study to study and from galaxy to galaxy. Typically upper limits of a few percent are estimated for the mean escape fraction at $z \lesssim 4$ (see Dayal et al. 2019; Robertson 2021, and references therein), with the notable exception of Steidel et al. (2018) who estimate an average $f_{\text{esc}} = 9\%$ at $z = 3$ (though the same sample of 124 galaxies was later estimated by Pahl et al. 2021 to have an average $f_{\text{esc}} = 6\%$). Most observational studies find little indication of a dependence on galaxy properties (Saxena et al. 2021) or redshift evolution (Meštrić et al. 2021) though there are exceptions such as Faist et al. (2016), who used measurements of oxygen line ratios to argue for both a galaxy mass dependency and a redshift evolution.

Indirectly, one can also constrain the global escape fraction, i.e. the total number of escaping over emitted LyC photons in the Universe, via the HI photo-ionization rate in the IGM, derived from the observed Ly α forest. By comparing this to the estimated intrinsic emission of LyC photons per volume from galaxies (and quasars, typically assuming unity escape fraction), UV background models derive a small $z \sim 3$ escape fraction of one or two percent (Haardt & Madau 2012; Khaire et al. 2015; Puchwein et al. 2019; Faucher-Giguère 2020; Yung et al. 2020). These same models however require at least a ten times higher global f_{esc} for $z \gtrsim 6$ in order to reionize the Universe. Therefore they postulate an evolving global escape fraction which is high during the EoR and decreases with redshift (see also Price et al. 2016, making similar predictions but with different methodology). Such a varying escape fraction with time is difficult to verify and to explain, though various authors have suggested that if it exists, it may be due to a redshift evolution towards more massive galaxies with lower escape fractions (Alvarez et al. 2012; Ferrara et al. 2012; Sun & Furlanetto 2015), towards more metal-rich galaxies with lower f_{esc} (Yoo et al. 2020), or a decreasing efficiency of stellar feedback in the expanding Universe in blowing out escape routes for the radiation (Sharma et al. 2017; Faucher-Giguère 2020; Ma et al. 2020).

The best theoretical approach we rely on to understand and predict f_{esc} is simulations. Most cosmological simulations of reionization aim for large volumes approaching cosmologically homogeneous scales on the order of hundreds of Mpc (e.g. Iliev et al. 2013; Gnedin 2014; Ocvirk et al. 2018; Kannan et al. 2021). These are very useful for understanding the overall process of reionization and make predictions for observable signals for different reionization scenarios. However, large volume comes at the cost of resolution and these simulations are far from resolving the propagation of radiation through the ISM, so f_{esc} is an input parameter rather than a prediction. Many works have used the zoom-simulation technique, where the evolution of one or a few galaxies is targeted in a cosmological environment, allowing for high enough resolution that the propagation of radiation through the ISM, and hence f_{esc} , can be predicted (e.g. Gnedin et al. 2008; Yajima et al. 2011; Wise et al. 2014; Ma et al. 2015, 2016; Kimm et al. 2017; Trebitsch et al. 2017). Other works forego the cosmological environment to gain even better resolution in idealised galaxies (e.g. Wise & Cen 2009; Yoo et al. 2020). A lot of discrepancies and disagreements remain between simulation works that predict f_{esc} , but the emerging picture is that escape fractions appear highly fluctuating but overall they decrease with increasing galaxy mass and metallicity, suggesting that reionization is disproportionately driven by low-mass metal-poor galaxies.

Except for a few existing works that either use large (Kimm & Cen 2014; Paardekooper et al. 2015; Xu et al. 2016; Trebitsch et al. 2021) or many (Ma et al. 2020) zoom regions, these zoom or idealised approaches are limited by the small number of simulated galaxies,

which prevents a systematic study of how escape fractions vary with galaxy properties such as mass, metallicity, and star formation activity. This limitation is amplified by the fluctuating nature of f_{esc} for individual galaxies which enhances the need for many objects in a statistical study. Additionally, the zoom and idealised galaxies approaches have the limitation that the reionization process is not modelled, making it difficult to tell how the predicted escape fractions translate to the reionization of the Universe. Also, the feedback effect of reionization on f_{esc} is not captured (e.g. Katz et al. 2020a; Ocvirk et al. 2021).

Armed with the SPHINX suite of simulations (Rosdahl et al. 2018) we aim for the best of both worlds: a large sample of tens of thousands of resolved galaxies evolving in non-zoomed cosmological simulations. The methods we have developed for SPHINX (Rosdahl et al. 2013; Rosdahl & Teyssier 2015; Katz et al. 2017; Rosdahl et al. 2018) unlock the goal of this paper: to statistically predict the escape of LyC radiation from EoR galaxies while self-consistently modelling the reionization history and high- z luminosity function, with unparalleled sample size and resolution. The simulation data provide us a mock Universe which reionizes at a reasonable redshift and in which we can measure the actual escape fractions, how they scale with various galaxy properties, which galaxies predominantly power reionization, and if – and if so, why – the global escape fraction evolves with time.

The setup of this paper is as follows. In Section 2 we introduce the SPHINX simulations used for the current analysis and recap their main characteristics. In Section 3 we present our results: we first compare to observational constraints for the luminosity function at various redshifts during the EoR (and hence the luminosity budget) and the reionization history. We present the redshift-evolution of the global escape fraction of LyC photons in SPHINX and show how f_{esc} scales with halo mass, galaxy mass, metallicity, magnitude, and specific star formation rate. We then show how galaxies with different properties contribute to the LyC luminosity budget during reionization and finally we probe what effects drive the redshift-evolution of f_{esc} in SPHINX. We discuss our results in Section 4 and present our conclusions in Section 5.

2 METHODS

The three cosmological radiation-hydrodynamical (RHD) simulations we use in this paper are part of the SPHINX project and extend the series presented in R18. With a few exceptions, the code and setup is identical here to that described in Rosdahl et al. (2018, hereafter R18). We refer the reader to R18 for a full description of the methods and parameters and highlight below the main characteristics of the runs used here.

2.1 Simulation code and setup

We use the RAMSES-RT code described in Rosdahl et al. (2013) and Rosdahl & Teyssier (2015). This is an RHD extension of the RAMSES parallel adaptive mesh refinement code (Teyssier 2002), adding radiative transfer and interactions of the radiation with gas to the cosmological hydrodynamics.

The initial conditions (ICs) for our periodic cosmological volumes are generated with MUSIC (Hahn & Abel 2011) using Λ CDM cosmological parameters compatible with the Planck Collaboration (2014) results. We minimise the effect of cosmic variance on the LyC luminosity budget by selecting the most “average” initial conditions for each of our volumes from a set of 60 ICs generated with MUSIC.

We assume constant and homogeneous H and He mass fractions of $X = 0.76$ and $Y = 0.24$ respectively. We use an initial homogeneous metal mass fraction of $Z_{\text{init}} = 6.4 \times 10^{-6} (= 3.2 \times 10^{-4} Z_{\odot})$, assuming a Solar metal mass fraction of $Z_{\odot} = 2 \times 10^{-2}$ throughout this work. This artificial and unrealistically non-zero initial metal mass fraction is necessary to allow gas to cool below $\approx 10^4$ Kelvin and collapse in the absence of H_2 formation from primordial gas, which is not modelled.

Our main simulation is a $(20 \text{ cMpc})^3$ (co-moving Mpc) volume, 8 times larger than the largest volume in R18. The other two simulations are smaller $(10 \text{ cMpc})^3$ volumes – using the exact same ICs as in R18 – which we study for completeness, one otherwise identical in setup to the main simulation, and one with a slightly different spectral energy distribution (SED) model (see below). All three simulations have the same resolution and refinement strategy. Dark matter (DM) particles have a mass of $m_{\text{DM}} = 2.5 \times 10^5 M_{\odot}$, with 512^3 particles in the smaller volume simulations and 1024^3 in the large one. We resolve halos at the atomic cooling mass of $3 \times 10^7 M_{\odot}$ (Wise et al. 2014) with 120 DM particles. The simulations have a minimum cell width of 10.9 pc at $z = 6$, having a co-moving finest cell width of 76.3 cpc, and a maximum cell width in the diffuse IGM of 2.8 kpc (19.6 ckpc) at $z=6$. Note that fixed co-moving maximum resolution means that the maximum physical resolution degrades linearly with the cosmological expansion factor a and the finest cell width doubles as a doubles, e.g. from $z = 11$ to $z = 5$.

We use adaptive refinement criteria to resolve dense and Jeans-unstable regions. A parent cell is split into 8 equal-size children cells if: i) $M_{\text{DM,cell}} + M_{\text{b,cell}}/f_b > 8 m_{\text{DM}}$, where $M_{\text{DM,cell}}$ and $M_{\text{b,cell}}$ are the total DM and baryonic (gas plus stars) masses in the cell and $f_b = 0.154$ is the baryon mass fraction; or ii) the local Jeans length is smaller than four local cell widths.

For the M1 radiative transfer (see Rosdahl et al. 2013), we use the variable speed of light approximation described in Katz et al. (2017) to speed up the calculation, such that the speed of light goes from 1.25% of the real speed of light in the highest resolution regions in the ISM to 20% in the coarsest cells representing IGM voids. We subcycle the radiative transfer within the hydro timestep to reduce the computational cost. Whereas we used three radiation groups in R18, for H I - He I - and He II -ionizing photons, we merge the two more energetic groups into one in the current simulations. This is done to reduce the number of radiation variables and hence mitigate the memory cost of the simulation. In Table 1 we show the energy ranges for the two photon groups as well as their typical energies and cross sections, which are updated regularly to reflect the “mean” stellar particles. Merging the two high energy (He I and He II) groups from R18 into one is acceptable because only a tiny fraction of the LyC photons emitted by stellar populations are in the highest energy (He II -ionizing) group, whereas the two lower-energy groups both contribute strongly in LyC (see Appendix D in R18 for details). It does not matter for H I and He I reionization whether one merges this highest energy group or simply omits it, and we have verified in post-processing that escape fractions are insensitive to whether the He II cross section is set to zero or our non-zero SED-derived value.

Another memory-saving change we make from R18 is to change the precision of all RHD cell variables from double to single precision, reducing the memory cost by almost half. We have performed idealised tests and smaller volume SPHINX runs to confirm that the reduction in precision has no effect on our results. We note that for all calculations, such as the radiation-hydro-gravity solver and thermochemistry, we cast the cell variables to double precision and then back to single precision when updating the cell state, to minimise the impact of numerical underflow and overflow.

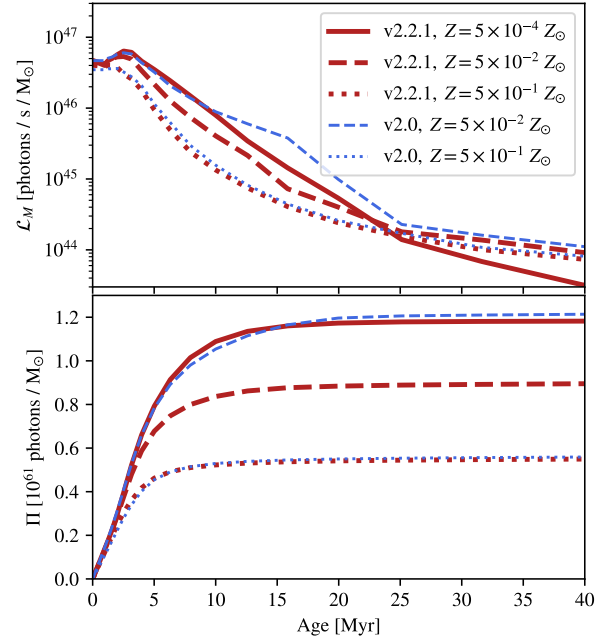


Figure 1. Ionising number luminosity (top) and cumulative number of ionising photons (bottom) per Solar mass with BPASS versions 2.2.1 and 2.0. Note that the very lowest metallicity, $5 \times 10^{-4} Z_{\odot}$, only exists in the newer model, while the older model starts at $5 \times 10^{-2} Z_{\odot}$. The newer model has significantly lower late-time luminosities for $Z \gtrsim 5 \times 10^{-2} Z_{\odot}$ than the older model at the same metallicities.

For stellar population LyC luminosities as a function of age and metallicity, we use the Binary Population and Spectral Synthesis model¹ (BPASS: Eldridge et al. 2007; Stanway et al. 2016; Stanway & Eldridge 2018), assuming a Kroupa (2001)-like initial mass function (IMF) with a slope of -1.3 from 0.1 to $0.5 M_{\odot}$ and -2.35 from 0.5 to $100 M_{\odot}$. For the fiducial run, which we name SPHINX²⁰ (the superscript referring to the volume width) we use BPASS version 2.2.1. This is an update from R18 where we used the older BPASS version 2.0. The newer version is extended to metallicities two orders of magnitude lower than in the older version, which is more representative for the metallicities of stellar populations formed in SPHINX. As shown in Fig. 1, the older version has significantly higher LyC luminosities than the new one for stellar populations older than a few million years and with low metallicities of $10^{-3} Z_{\odot} \lesssim Z \ll Z_{\odot}$.

As shown in R18, the escape of LyC radiation from galaxies is highly sensitive to subtle variations in the assumed SED model, especially at advanced stellar population ages and low metallicities. Indeed, as demonstrated later in this paper, using the two BPASS versions in otherwise identical simulations leads to very different reionization histories that bracket observational constraints, with the older version giving much earlier reionization than the newer one. Therefore we analyse simulations using each version. Performing two runs with the volume size of SPHINX²⁰, however, is prohibitively expensive, so we report on two smaller-volume simulations: SPHINX¹⁰_{early} (because it reionizes early) is a $(10 \text{ cMpc})^3$ volume where we use the older BPASS version 2.0, and SPHINX¹⁰ is the same volume, but with BPASS 2.2.1, to provide a clean comparison to SPHINX¹⁰_{early} (i.e. sep-

¹ <https://bpass.auckland.ac.nz>

Table 1. Photon group energy (frequency) intervals and properties. The energy intervals are indicated in units of eV by ϵ_0 and ϵ_1 and in units of Ångström by λ_0 and λ_1 . The last four columns show photon properties derived every 10 coarse time-steps from the stellar luminosity weighted SED model. These properties evolve over time as the stellar populations age, and the approximate variation is indicated in the column headers (the difference being similar in the two SED models we use). $\bar{\epsilon}$ denotes photon energies while σ_{HI} , σ_{HeI} , and σ_{HeII} denote cross sections for ionization of hydrogen and helium and helium, respectively.

Photon group	ϵ_0 [eV]	ϵ_1 [eV]	λ_0 [Å]	λ_1 [Å]	$\bar{\epsilon}$ [eV] ±20%	σ_{HI} [cm ²] ±10%	σ_{HeI} [cm ²] ±10%	σ_{HeII} [cm ²] ±25%
UV _{HI}	13.60	24.59	9.1×10^2	5.0×10^2	18.3	3.2×10^{-18}	0	0
UV _{He}	24.59	∞	5.0×10^2	0	33.9	6.2×10^{-19}	4.7×10^{-18}	1.5×10^{-21}

Table 2. Simulations used in this work. From left to right: simulation name, volume width, and SED model used for stellar population LyC luminosities.

Name	L_{box} [cMpc]	SED model
SPHINX ²⁰	20	BPASS v2.2.1
SPHINX ¹⁰	10	BPASS v2.2.1
SPHINX ¹⁰ _{early}	10	BPASS v2.0

arating the effects of changing the SED model and the cosmological volume). The simulations are listed in Table 2.

A stellar LyC luminosity factor is often applied in RHD simulations of reionization, to account for either unresolved absorption of radiation (factor <1) or unresolved channels through which the radiation can escape (factor > 1), and calibrated to match observational constraints of the reionization history. This factor is unity in all SPHINX simulations presented here, i.e. stellar particles inject into their host cells the luminosities given by the assumed SED model, and our escape fractions emerge as the ratio of the rate of photons escaping a halo versus its total LyC luminosity. This does not mean, however, that our simulations resolve the transport of radiation on the smallest scales and we indeed demonstrate later in the paper that our overall escape fractions are not converged with resolution and are likely somewhat under-predicted compared to reality. It simply happens, as we will show, that our combination of resolution, sub-grid models, and assumed stellar evolution models, produces a fairly realistic model of the early Universe and its reionization and hence presents a plausible model to probe how radiation escapes from galaxies with different properties and which galaxies predominantly contribute to reionization.

Gas cooling and heating is described in detail in Rosdahl et al. (2013). The non-equilibrium hydrogen and helium thermochemistry is coupled with the local ionizing radiation and evolved semi-implicitly via collisional ionisation, collisional excitation, photo-ionization, recombination, bremsstrahlung, Compton cooling off cosmic microwave background radiation, and di-electric recombination. The non-equilibrium abundances of HI, HII, HeI, HeII, and HeIII are tracked and stored in each gas cell. For $T > 10^4$ K, additional cooling rates from heavier elements are pre-calculated from Cloudy (Ferland et al. 1998), assuming photo-ionization equilibrium with a redshift-evolving UV background. For $T \leq 10^4$ K we use fine structure metal cooling rates from Rosen & Bregman (1995), allowing the gas to cool to a temperature floor of 15 K.

Star formation is performed with the thermo-turbulent model described in R18. Gas cells are eligible for star formation only if the local hydrogen density $n_{\text{H}} > 10 \text{ cm}^{-3}$, the local turbulent Jeans length is smaller than the finest cell width, and the gas is locally convergent. If a cell is eligible for star formation under these conditions, its gas is converted stochastically into stellar particles as described by Raseria & Teyssier (2006), and its star formation efficiency is

a non-linear function of the local virial parameter and turbulence (Federrath & Klessen 2012). The stellar particles, representing co-eval stellar populations, have an initial mass of $400 M_{\odot}$, somewhat smaller than the $1000 M_{\odot}$ particles in R18.

Supernova (SN) feedback is also unchanged from R18. Stellar particles undergo individual 10^{51} erg explosions from an age of 3 to 50 Myrs. Injection of energy and momentum from those individual SN explosions is performed with the “mechanical” feedback model described in e.g. Kimm et al. (2015), where the energy is injected thermally if the resolution is sufficient to correctly capture the Sedov-Taylor expansion. Otherwise, to overcome direct numerical overcooling, a physically motivated density- and metallicity-dependent amount of momentum is injected, which has been derived from high-resolution numerical experiments. SN explosions from a stellar particle are sampled in time to produce an average mass return of 20 percent of the original stellar mass back into the ISM, a metal yield of 0.075, and an average of 4 SN explosions per $100 M_{\odot}$. The mass return is close to that of a Kroupa (2001) IMF, and therefore consistent with the BPASS model. However, the number of SN explosions per Solar mass is boosted roughly four-fold compared to Kroupa (2001). This calibrated and artificial boost in the number and total energy of SN explosions is necessary to suppress star formation enough to produce a realistic high-redshift luminosity function. The necessity of such a boost in SN feedback is still not fully understood and reflects an important unsolved question in galaxy formation, where simulated galaxies tend to form stars too efficiently compared to observations. It may be due to a lack of additional ill-understood feedback channels such as cosmic rays (e.g. Farcy et al. 2022), or to insufficient resolution to self-consistently model a multi-phase turbulent ISM.

To recap, the differences in setup from R18 are less massive stellar particles, single precision RHD, two radiation groups (reduced from three), and, most significantly, an updated BPASS version for stellar LyC luminosities in our fiducial SPHINX²⁰ run.

At the end of the run at $z = 4.64$, SPHINX²⁰ contains about 5×10^9 cells and a billion stellar particles. The run, performed on 10,080 cores, required about 50 million core-hours. We write simulation outputs every 5 Myrs, giving a total of 216 outputs between $z = 20$ and the end at $z = 4.64$. The size per output increases significantly from start to finish due to structure formation and increasing AMR refinement, being about 350 GB at the beginning and 1.2 TB at the end, and the total size of all output is 105 TB. The two smaller volume simulations have been performed on 2,880 cores and require roughly a tenth of the memory and CPU-time compared to SPHINX²⁰.

2.2 Halos and escape fractions

To identify dark matter halos, we use the ADAPTAHOP halofinder (Aubert et al. 2004; Tweed et al. 2009) on the dark matter particles, using the same parameters as described in R18.

We associate stars to halos as follows. Each stellar particle is assigned to the closest (sub-) halo, using the weighted distance measurement $d = r/R_{\text{vir}}$, where r is the distance between the particle and the halo centre and R_{vir} is the virial radius of the halo. A stellar particle with $d > R_{\text{vir}}$ for any halo is not assigned at all. Such unassigned stellar particles do exist, but they are negligible in both number and ionizing luminosities, even if we assume all their radiation escapes into the IGM. We do not assign stars to sub-halos fully enclosed within R_{vir} of their parent halo (i.e. stars within the sub-halo are assigned to its parent halo).

We compute LyC and 1500 Å escape fractions from halos in post-processing using the Monte-Carlo radiative transfer code RASCAS (Michel-Dansac et al. 2020). We prefer to use ray-tracing to measure escape fractions rather than using the M1 radiation fluxes in the simulation outputs directly, as our variable speed of light generates significant and variable delays between the emission of radiation and escape at R_{vir} that are difficult to track. Furthermore, ray-tracing allows us to individually measure escape fractions from each stellar particle. Trebitsch et al. (2017) showed, using the same methods but with a constant speed of light, that RASCAS yields almost identical escape fractions as using the M1 flux directly. Contrary to R18 where we obtained galaxy escape fractions by computing the optical depth along 500 rays from each star particle, here we use a Monte Carlo sampling technique, where we cast photon packets from star particles with a probability proportional to their LyC luminosity. These photon packets are propagated with RASCAS until either they escape the virial radius of the host halo or are absorbed by an H or He atom. The escape fraction is then the fraction of photon packets which reached R_{vir} without being absorbed. We set the number of photon packets per halo to be 100 times the number of star particles, with a minimum of 10^4 and a maximum of 10^7 . We have checked that the resulting escape fractions are converged and accurate to sub-percent relative precision regarding the number of photon packets. Our results are also insensitive to our choice of R_{vir} as the escape distance, which is rather arbitrary but commonly used in the simulation literature to measure escape fractions. We have tested using instead both $2R_{\text{vir}}$ and 10 kpc from each photon source (the latter corresponding to the virial radius for $M_{\text{vir}} \approx 10^{10} M_{\odot}$ halos at $z \sim 6$) and found that the measured escape fractions are also sub-percent converged. Note that for consistency, we repeat here the RAMSES-RT approximation and bin radiation in two frequency bins with mean cross sections, and the total escape fraction of a galaxy is the LyC-luminosity-weighted mean of that of the two radiation groups. For reference, Mauerhofer et al. (2021) compute escape fractions by propagating the full spectra with RASCAS, which gives similar results within a few percent relative precision (Valentin Mauerhofer, private comm.).

Throughout the paper, the sample of halos considered is the full population of galaxies, i.e. any halo hosting stellar particles, without any threshold on its star formation rate. The LyC escape fraction considered is always the intrinsic-LyC-luminosity weighted (not number-weighted) mean escape fraction of all halos or halos with a given property, or equivalently the fraction of LyC photons emitted that escapes into the IGM.

For attenuated 1500 Å (or UV) luminosities of galaxies embedded in DM halos, we use the same Monte-Carlo routine to derive UV escape fractions, but here with absorption by dust instead of hydrogen and helium. We use the formulation of Laursen et al. (2009), assuming that the dust absorption coefficient scales linearly with the local metal mass fraction of the gas and the neutral hydrogen density, as also described in Garel et al. (2021). The UV escape fraction is then found as described above, but using 1500 Å luminosities for the stellar particles, as provided by the assumed SED model.

For the LyC radiation we ignore absorption by dust. This is for consistency with the on-the-fly absorption in the simulation itself, where dust is also ignored. Dust absorption of LyC radiation is expected to be negligible (Yoo et al. 2020) because the dust optical depth, while not necessarily always small, is always much smaller than the photo-ionization optical depth (Mauerhofer et al. 2021). We have verified this by calculating escape fractions with dust absorption in post-processing for a few of the last snapshots in SPHINX²⁰, using the same formulation for dust as described above. These tests indeed reveal that the largest effect of dust on f_{esc} is in UV-bright galaxies that already have very low escape fractions via atomic absorption, and that the effect on mean escape fractions, at any UV brightness, is negligible. A deeper analysis on the effect of dust on LyC escape fractions in SPHINX will be presented in Katz et al. in prep.

3 RESULTS

The central panel of Fig. 2 shows a projection of the full SPHINX²⁰ volume at $z = 6$ in gas density (green), temperature (red), photo-ionization rate (white), and neutral fraction (purple). Smaller panels in the same figure show zoomed-in projections of neutral hydrogen column density and photo-ionization rate for some of the individual galaxies, with panel widths corresponding to 20 percent of the parent halo radius. The bottom-row of panels shows different low-mass galaxies at $z = 6$, residing in halos with $M_{\text{vir}} \approx 10^9 M_{\odot}$, while the other zoom-in panels show some of the most massive galaxies at the same redshift, with halo masses in the range $10^{10} - 10^{11} M_{\odot}$. The simulation produces a wide range of galaxy masses and morphologies due to different environments and accretion histories. At $z = 6$, the simulation contains ≈ 32 thousand star-forming halos, i.e. halos containing one or more stellar particles, ≈ 57 thousand resolved halos with $M_{\text{vir}} > 7.5 \times 10^7 M_{\odot}$, and ≈ 454 thousand halos identified by the halofinder with 10 DM particles or more.

The bottom row galaxies represent four stages typically found for low-mass galaxies in SPHINX, in a looping sequence going from left to right: i) gas accumulation with inefficient star formation (SF) – and hence low LyC luminosity – and low f_{esc} on the far left, ii) onset of star formation, with efficient SF and low f_{esc} in the second panel from left, iii) disruptive feedback with still-high SF and high f_{esc} in third and fourth panels from left, and iv) total disruption, with high f_{esc} but inefficient SF in the two rightmost panels. A low-mass galaxy can remain in that last stage for tens of millions of years, but eventually starts accumulating gas again and repeats the cycle, starting again at stage i).

We split our results into several sections. We first demonstrate that the simulated galaxies realistically represent actual high- z galaxies via comparing their properties to available observational constraints and show that they power reionization in a reasonable timeline. We then show the evolution of the global escape fraction with redshift. We go on to investigate trends of ionizing escape fractions with halo properties and which halos dominate the budget of ionising radiation reaching the IGM. Finally we investigate the evolution of the global escape fraction with time.

3.1 UV luminosity function

To establish that our SPHINX²⁰ simulation forms stars at approximately the correct rate, we start with the UV luminosity function at 1500 Å in SPHINX²⁰, shown in Fig. 3 at integer redshifts from $z = 5$ to $z = 10$. The dashed and solid red curves show the simulated intrinsic and dust-attenuated LFs, respectively, with dust-attenuation

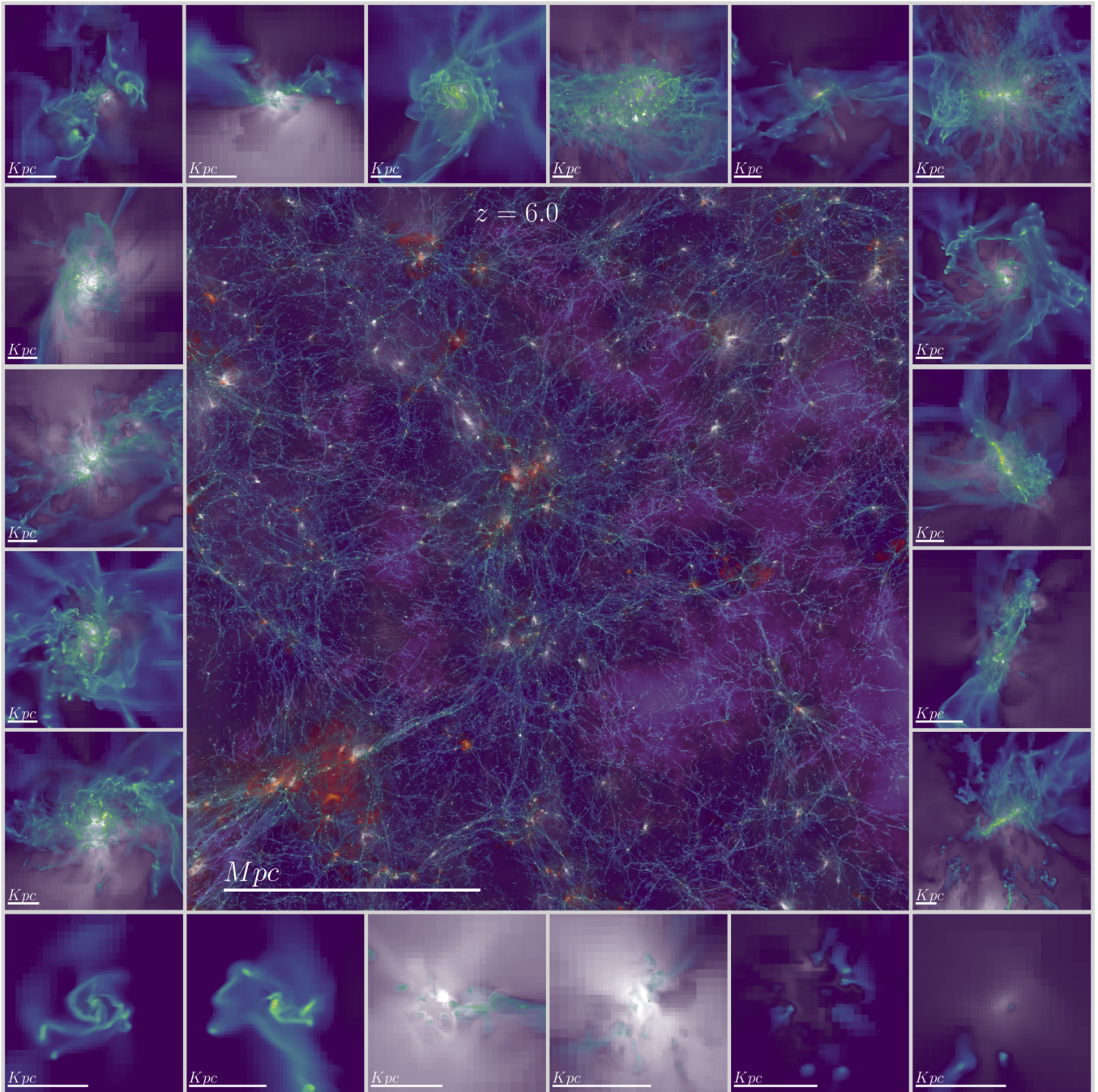


Figure 2. Galaxies from SPHINX²⁰ at $z = 6$. The large central panel shows a projection of the full simulation volume, with green filaments and clumps showing gas density, red denoting hot outflows ($T \gtrsim 10^5 K$) driven by SN feedback, white denoting intense hydrogen photo-ionization rates Γ_{HI} , and purple denoting islands of still-neutral hydrogen. The smaller panels show individual galaxies, with green denoting neutral hydrogen column density N_{HI} and white denoting Γ_{HI} , with the same ranges in all the small panels of $N_{\text{HI}} = 10^{20.5} - 10^{24.5} \text{ cm}^{-3}$ and $\Gamma_{\text{HI}} = 10^{-13} - 10^{-7} \text{ s}^{-1}$. The length scale is shown in the bottom left corner of each panel. The bottom row of panels shows halos with virial mass $M_{\text{vir}} \approx 10^9 M_{\odot}$, while other panels show some of the most massive halos at $z = 6$, with $M_{\text{vir}} = 10^{10} - 10^{11} M_{\odot}$. SPHINX galaxies have a wide range of morphologies and properties, some emitting a lot of LyC photons into the IGM and others not.

taken into account using the method described in §2.2. Compared to the intrinsic LF, the attenuated LF is shifted to dimmer magnitudes primarily at the bright end, by up to two dex. This strong attenuation at the bright end is expected, since the brightest galaxies tend also to be the most metal-enriched and hence dusty ones.

We include at each redshift a sub-set of published observational limits, as indicated by the legends. At $z = 5$ we show results from

Bouwens et al. (2015); Finkelstein et al. (2015) using different combinations of Hubble Space Telescope (HST) surveys. At higher redshifts we show results from works using the Hubble Frontier Fields (HFF) clusters, which magnify the high- z sources via lensing: Livermore et al. (2017, two HFF clusters), Bouwens et al. (2017, four HFF clusters), Atek et al. (2018, 6 HFF clusters), Atek et al. (2015, three HFF clusters); Ishigaki et al. (2017, six HFF clusters), and

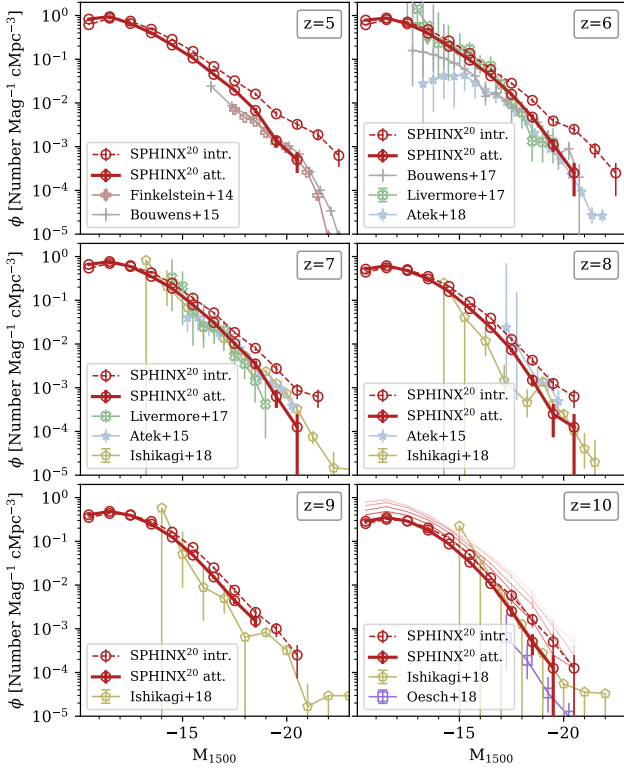


Figure 3. 1500 Å UV luminosity function at different redshifts, as indicated in the top right corner of each panel, from SPHINX²⁰ and observations, as indicated in the legends. For SPHINX²⁰, intrinsic (dust-attenuated) luminosities are shown in dashed (thick solid) red curves. To clearly show the evolution of the simulated LF, we re-plot the attenuated SPHINX²⁰ LF from other panels in the bottom-right z=10 panel, with decreasing redshift represented by increasingly light red color. We use Poissonian error-bars for the SPHINX data (but note that the error from cosmic variance is typically larger). The simulated LF agrees well with observational limits at all redshifts shown, implying a realistic intrinsic LyC volume-emissivity during the simulated EoR.

Oesch et al. (2018, six HFF clusters, plus legacy HST datasets). All these observational results have large uncertainties due to lensing model assumptions, cosmic variance, and small sample sizes. This can be seen from the error bars in Fig. 3 as well as in the difference between individual observational analyses, which use different models and/or model parameters. The attenuated SPHINX²⁰ luminosity function mostly falls within the range of observational data, though it does tend to be on the high side of that range, and therefore is in good agreement with observational constraints. The same is true for the smaller volume SPHINX simulations we report on. They have almost identical UV luminosity functions as shown here for SPHINX²⁰, except that they are cut off at dimmer magnitudes, being smaller volumes, and hence agree equally well with observations. This similarity in the UV luminosity function between simulations with different BPASS versions is because star formation is insensitive to the assumed SED model and the two SED models have very similar 1500 Å intensities, even if LyC intensities vary. The simulations thus provide a good working model of the high-redshift Universe through which we can explore the production and escape of ionizing radiation from galaxies².

² We note also that Garel et al. (2021) have shown good agreement of SPHINX with the extreme-z Lyman-alpha luminosity function, though here there is

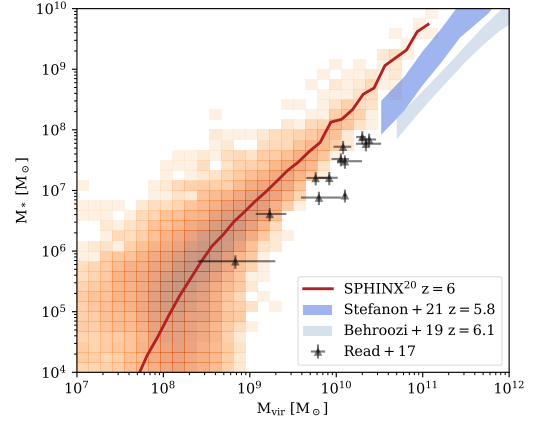


Figure 4. Stellar mass to halo mass relation in SPHINX²⁰ at $z = 6$. The red solid curve shows mean stellar mass per halo mass bin. The orange pixels show the distribution in stellar mass on a logarithmic color scale, with the lightest pixels containing single halos and the darkest containing about a thousand. The shaded areas in the upper right corner show $z \approx 6$ abundance matching constraints from Stefanon et al. (2021a) and Behroozi et al. (2019), and black triangles show observational constraints of $z = 0$ isolated dwarf galaxies (Read et al. 2017).

3.2 Stellar mass to halo mass

We consider in Fig. 4 the stellar mass to halo mass (SMHM) relation of SPHINX²⁰ galaxies at $z = 6$, compared to the abundance matching constraints of Stefanon et al. (2021a) and Behroozi et al. (2019) at similar redshifts and observational estimates for local dwarf galaxies from Read et al. (2017). We do not show the SMHM relations for the smaller SPHINX volumes here, but they are very similar except for not having as massive halos. The SPHINX²⁰ galaxies show a wide scatter in stellar mass for the lower-mass halos, but this scatter shrinks with increasing halo mass. Where there is overlap in halo mass, the SPHINX stellar masses are a factor of a few larger than those derived from abundance matching by Stefanon et al. (2021a), and a bit further away from the results of Behroozi et al. (2019). This suggests that SPHINX galaxies may be somewhat too star-forming, although it is non-trivial to align this discrepancy with the good agreement shown in Fig. 3 between SPHINX and the observed luminosity function at various redshifts.

We note that the stellar masses reported here for SPHINX²⁰ are a few tens of percent higher than for the smaller volume SPHINX simulations described in R18. This is due to the more inclusive way we assign stars to halos in the current paper: here we assign all stars within a halo, whereas in R18 we used a galaxy finder algorithm on the stellar particles to identify galaxies, which tends to exclude satellites and diffuse stellar distributions in the halo. The latter method is closer to the spirit of observations, but we prefer the former here, since it is how we assign stars to halos throughout the paper to compute escape fractions.

3.3 Reionization

We now compare the simulated reionization histories against observational constraints. We show in Fig. 5 the reionization history of

little overlap between the low-luminosity range of simulations and high-luminosity range of observations.

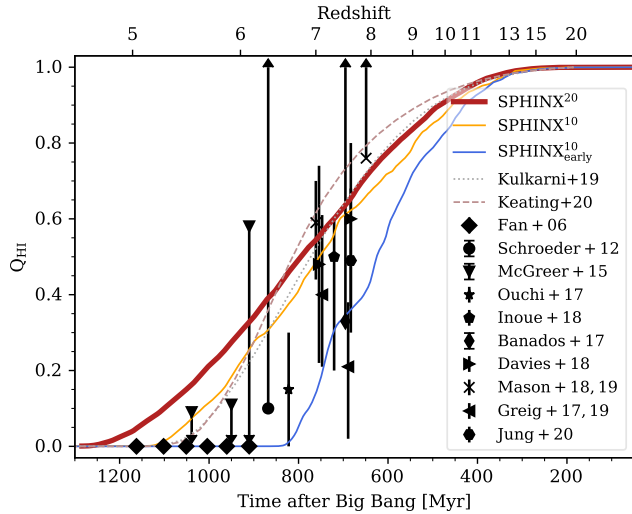


Figure 5. Evolution of the volume-filling neutral hydrogen fraction in three SPHINX runs (solid curves). The thick solid red curve represents the fiducial SPHINX²⁰ run we focus on in this work. For comparison we show observational estimates from Fan et al. (2006a), Schroeder et al. (2012), McGreer et al. (2015), Ouchi et al. (2017), Inoue et al. (2018), Bañados et al. (2017), Davies et al. (2018), Mason et al. (2018), Mason et al. (2019), Greig et al. (2017), Greig et al. (2019), and Jung et al. (2020), as indicated in the legend. We also show the late reionization scenarios from Kulkarni et al. (2019) and Keating et al. (2020). The timing of reionization is very sensitive to small variations in the SED model (solid blue vs. solid orange) and somewhat sensitive to the cosmological ICs (solid red vs. solid orange).

our fiducial SPHINX²⁰ simulation (thick solid red curve) in the form of the volume-weighted neutral fraction, Q_{HI} , versus redshift. We include the same for the two smaller volume simulations, SPHINX¹⁰ (same SED model) and SPHINX¹⁰_{early} (brighter SED model). The updated BPASS version 2.2.1 we use in this work for SPHINX²⁰ and SPHINX¹⁰ has about 30 percent less total ionising radiation emitted over the lifetime of an extremely metal-poor stellar population than the older version 2.0 used in SPHINX¹⁰_{early} and a factor ≈ 4 lower ionising luminosity at a stellar population age of ≈ 15 Myr (see Fig. 1).

The SPHINX²⁰ simulation achieves full reionization ($Q_{\text{HI}} = 10^{-3}$) at $z = 4.64$. This is quite late compared to the various existing observational estimates shown with black symbols in Fig. 5, and well beyond the standard scenario of reionization by $z=6$ (Fan et al. 2006b). However, large variations are expected in volumes as small as ours and besides, SPHINX²⁰ reionization is not very far from *late reionization* scenarios proposed recently by Kulkarni et al. (2019) and Keating et al. (2020), shown in dotted curves.

Switching to an 8 times smaller volume than SPHINX²⁰ but otherwise identical setup, SPHINX¹⁰ is fully reionized about 150 Myrs earlier (orange solid curve), or at $z = 5.1$. This is presumably somewhat random and due to cosmic variance, i.e. slightly different halo mass functions between the two simulations. Now switching from SPHINX¹⁰ to SPHINX¹⁰_{early}, which uses BPASS version 2.0 but is otherwise identical, we find a large effect on reionization, which is achieved about 300 Myrs earlier with the older SED version, or at $z = 6.5$. Such sensitivity to the assumed SED model has already been demonstrated in Ma et al. (2016) and Rosdahl et al. (2018).

The latest constraints of the Thomson optical depth $\tau = [0.0471, 0.0617]$, reported in Planck Collaboration et al. (2018),

almost precisely bracket the three SPHINX simulations, with $\tau = 0.049, 0.052$, and 0.061 in SPHINX²⁰, SPHINX¹⁰, and SPHINX¹⁰_{early} respectively (calculated from the redshift evolution of the hydrogen and helium ionization fractions using eq. 6 in Zaroubi et al. 2012).

The three SPHINX simulations used here produce reionization histories that bracket most observational constraints and recent models. Even though the SPHINX²⁰ simulation pushes a bit even the recent late-reionization models, we still prefer to focus our analysis in the current paper on this simulation, since it has almost an order of magnitude better statistics – i.e. more galaxies – and an order of magnitude more massive galaxies than the smaller volumes. Both these aspects are very important for a meaningful statistical study of the escape of ionising radiation from galaxies, due to its enormous variability over time and from one galaxy to another. We show in Appendix B how our main results vary with different volume size and BPASS version, and to summarise we find that the correlations we study as well as our conclusions are insensitive to those factors.

Any reionization model has degeneracies in f_{esc} , star formation, and the amount of LyC photons produced per stellar mass, and none of those factors are very well constrained (although the uncertainties on f_{esc} are probably the largest). Models with different combinations of these three factors, within reasonable limits, may be equally successful in reproducing observational constraints of the reionization history and high- z luminosity functions. Indeed we find different SPHINX simulations can have different f_{esc} and yet bracket the aforementioned observational constraints. Therefore this work is not very predictive on the overall magnitudes of escape fractions, which can plausibly be larger than what we find in this work, combined with somewhat lower star formation rates and/or more conservative SED models. Our goal is not to predict the magnitudes but rather how escape fractions correlate with galaxy properties and how they may evolve with redshift. These correlations, which we will demonstrate to be well converged with resolution, volume size, and SED models considered, should be the take-away message of this paper.

3.4 Global LyC escape fraction

We now examine the global LyC-luminosity weighted escape fraction f_{esc} of LyC photons in the simulated volumes. We show the redshift-evolution of f_{esc} in the three SPHINX simulations in Fig. 6. Thin solid transparent curves show instantaneous f_{esc} while the corresponding thick opaque curves show their sliding luminosity-weighted average over the last 100 Myrs, or $f_{\text{esc},100}$. We note the following observations from the figure:

(i) Even if averaged over up to two billion stellar particles and tens of thousands of halos in SPHINX²⁰, the instantaneous escape fraction fluctuates strongly over time, and even more so in the smaller volume simulations. We focus for now on $f_{\text{esc},100}$, where the difference between simulations is easier to assess.

(ii) The escape fraction is significantly ($\approx 50 - 100\%$) higher for the older and brighter BPASS version 2.0 SED model (blue) than for the identical simulation volume with the fiducial version 2.2.1 (orange). This partly explains the earlier reionization with the older version shown in Fig. 5 (complementary to the higher intrinsic stellar luminosities in the older version). We address in §4.1 why the more luminous SED model results in higher escape fractions.

(iii) The escape fraction is lower for the larger (20 cMpc)³ volume (red) than for the smaller (10 cMpc)³ volume (orange), even if both use the same SED model. We address this difference in §4.2.

(iv) The global escape fraction decreases with time. For the SPHINX²⁰ volume, it goes from just under 10 percent at $z = 15$

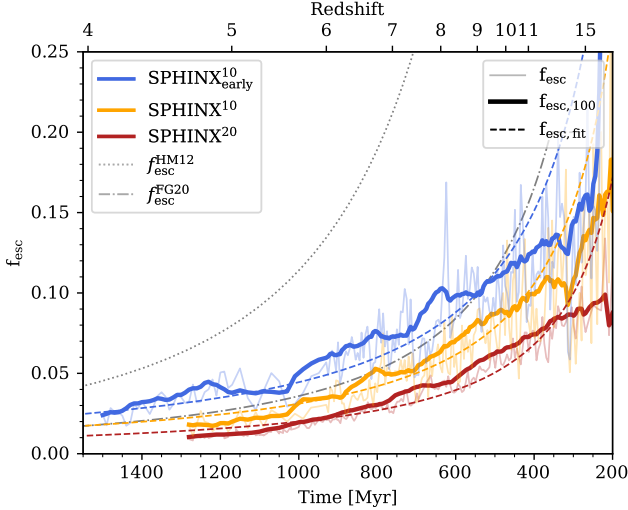


Figure 6. Time-evolution of the global (luminosity-weighted) escape fraction f_{esc} in the three SPHINX simulations. The transparent highly fluctuating f_{esc} curves are instantaneous escape fractions, while the opaque thick curves show sliding luminosity-weighted averages over the previous 100 Myrs. Dotted and dash-dotted grey curves show the models from Haardt & Madau (2012) and Faucher-Giguère (2020), respectively, to demonstrate how a trend of decreasing f_{esc} with redshift is typically assumed in reionization models. The thin dashed curves show our fits to the global f_{esc} evolution in the three SPHINX simulations to the functional form used by Haardt & Madau (2012), $f_{\text{esc}}(z) = a(1+z)^b$, with $a = 4.5 \times 10^{-4}$, 7×10^{-4} , and 10^{-3} for SPHINX²⁰, SPHINX¹⁰, and SPHINX^{10_early}, respectively, and $b = 2$ in all cases. The global escape fraction in SPHINX decreases with time, as required to reionize the high-redshift Universe while simultaneously reproducing the observational constraint of very low escape fractions at low redshift.

to about one percent at $z = 5$, and a qualitatively similar evolution is seen in the other SPHINX simulations. A drop in f_{esc} with time is almost always assumed by empirical reionization models, two of which are shown in dotted and dashed curves in Fig. 6 for reference (eq. 56 in Haardt & Madau 2012 and eq. 12 in Faucher-Giguère 2020, though note these empirical models can vary greatly in the overall magnitudes due to aforementioned degeneracies with star formation rates and stellar LyC luminosities as well as uncertainties in the timing and duration of reionization). Different physical reasons for what drives such a drop have been suggested, but none confirmed. The SPHINX simulations naturally produce a drop in f_{esc} with redshift, in qualitative agreement with empirical reionization models, and we address in §3.7 what drives this evolution.

(v) The escape fraction we find is low, well below 10% during most of the EoR. While this is at odds with some values used in the literature (e.g. 20% in Ouchi et al. 2009 or the Haardt & Madau 2012 model shown in Fig. 6), it is very consistent with the recent model of Faucher-Giguère (2020) included in Fig. 6, as well as with Finkelstein et al. (2019) in whose model an average $f_{\text{esc}} < 5\%$ is sufficient to reionize the Universe.

The average f_{esc} at a given time as shown in Fig. 6 does not represent the escape fraction in a typical halo in the simulation. Rather, most halos have almost zero f_{esc} and/or negligible intrinsic luminosities, while a tiny fraction of halos have high f_{esc} and non-negligible luminosities simultaneously. At a given time, the escaping ionising emissivity is hence typically dominated by a small fraction of halos, which explains the large fluctuations in the global f_{esc} in

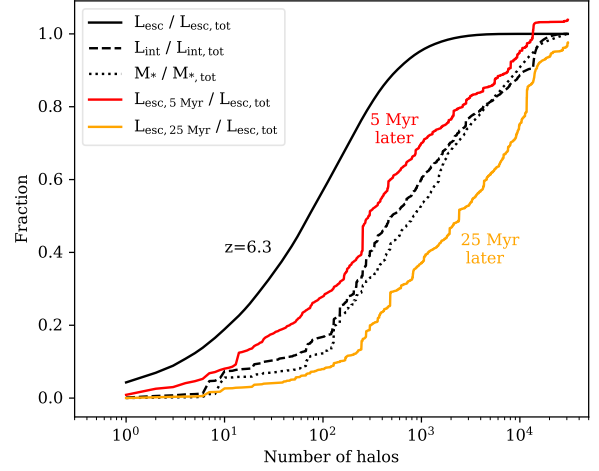


Figure 7. Fraction of total escaping and intrinsic LyC luminosities, in solid and dashed black respectively, from individual halos in a single snapshot at $z = 6.3$ in SPHINX²⁰, ordered by decreasing escaping halo luminosity. The dotted black curve shows the cumulative stellar mass fraction of the same halos and in the same order. The escaping LyC emissivity in the simulated volume is dominated by a relatively few halos, with only about 100 halos out of $\approx 3 \times 10^4$ being responsible for almost 60 percent of the escaping emissivity, and about 95 percent of the escaping emissivity coming from a thousand halos. The red and orange curves show the cumulative escaping emissivity from the same halos in the same order 5 and 25 Myrs later. The escaping emissivities of individual galaxies change rapidly and dramatically, with the 100 previously most dominant halos accounting for only about a quarter and the tenth of the escaping photons 5 and 25 Myrs later. Note that the red and orange curves are normalised to the total escaping luminosity at $z = 6.3$, which is why they do not converge to unity. In other words, the total escaping emissivity changes over time.

Fig. 6. In addition, due to the stochasticity of both star formation and escape fractions for individual halos, this situation changes rapidly, with the halos that dominate the escaping emissivity at a given time becoming sub-dominant only a few million years later. Reionization of the SPHINX volumes is “disco-like”, as coined by Matthee et al. (2021), with galaxies emitting brief flashes of LyC radiation into the IGM and then going dark.³

We demonstrate this in Fig. 7. Here we show the fractions of the total escaping emissivities in SPHINX²⁰ in solid black at $z = 6.3$, ordering the halos by decreasing escaping luminosity, i.e. with the LyC-brightest halos on the left. Out of the $\approx 3 \times 10^4$ halos containing stars, a single halo contributes almost 5 percent of the total escaping emissivity L_{esc} , 10 halos contribute to ≈ 20 percent of it, and 100 halos to ≈ 60 percent. These contributions are quite different from the *intrinsic* emissivities, L_{int} , shown in dashed black, with e.g. the 100 L_{esc} -brightest halos contributing to $\lesssim 20$ percent of L_{int} . This is because halos with similar intrinsic luminosities can exhibit very different escape fractions. Both the escape fractions and luminosities vary dramatically over time. The solid red and orange curves show the fraction of L_{esc} for the same halos and in the same order, 5 and 25 Myrs later, respectively. The 10 halos that contributed to ≈ 20 percent of the total L_{esc} at $z = 6.3$ contribute 25 Myrs later to about

³ Readers are encouraged to experience disco-reionization animations on the SPHINX website: <http://sphinx.univ-lyon1.fr>. Disco music is not provided, so please bring your own.

2 – 3 percent of the total, and the 100 halos that contributed $\approx 60\%$ earlier now contribute $\approx 10\%$.

Given the large time-variability in escape fractions and LyC emissivities, we find it both reasonable and necessary to stack simulation snapshots in most of the forthcoming analysis of escape fractions and relative contributions of halos to the escaping emissivity. For each redshift interval, we collect data from all snapshots within that interval, always having 5 Myrs between individual snapshots. We therefore treat a single halo, evolving over time, as many. Without such stacking, the combination of small statistics and large scatter leads to excessive noise when binning escape fractions by halo (or galaxy) properties, as we do in the next sections.

3.5 Escape of LyC photons from halos

We now assess how LyC escape fractions correlate with several halo properties. We consider halo mass (M_{vir}), stellar mass (M_*), metallicity (Z_{halo}) and specific star formation rate (sSFR), each of which has been predicted by different theoretical works to have an effect on the escape fraction, and also UV magnitude (M_{1500}), in order to estimate the fraction of escaping LyC photons which are accounted for in the bright and well-constrained part of the high- z luminosity function.

3.5.1 Halo mass

We show in Fig. 8 how LyC escape fractions correlate with halo mass M_{vir} at different redshifts. Each panel covers a redshift interval, with the highest redshifts in the top left panel and the lowest redshifts in the bottom right one. For each redshift interval, we plot the LyC-luminosity-weighted mean escape fraction per halo mass in blue, and we show the intrinsic-luminosity-weighted probability distribution of f_{esc} in the background to illustrate the scatter for individual halos. We also show in red the fraction of total intrinsic LyC luminosity produced by halos below a given mass and in purple the corresponding *escaping* luminosity (which is just the product of the blue and red curves). In each panel we stack all snapshots belonging to the relevant redshift range in order to reduce the noise.

Several insights can be drawn from Fig. 8. Firstly, at all simulated redshifts, we find a fairly flat f_{esc} for all halos with $M_{\text{vir}} \lesssim 3 \times 10^9 M_{\odot}$ and a drop in f_{esc} for more massive halos. This drop for high halo (or galaxy) masses is not particularly surprising and a similar feature has been reported in several works (Razoumov & Sommer-Larsen 2010; Kimm & Cen 2014; Paardekooper et al. 2015; Xu et al. 2016; Yajima et al. 2020; Ma et al. 2020; Lewis et al. 2020), though there is not full agreement on this point and some have predicted the opposite trend (Gnedin et al. 2008; Wise & Cen 2009; Naidu et al. 2019). The reason for the drop in f_{esc} with increasing halo mass is that stellar feedback gradually becomes less efficient with mass in clearing out gas and allowing radiation to escape. While most recent works agree that the escape fraction decreases at high halo masses, there is no agreement on the magnitudes of escape fractions or the halo mass limit at which the escape fraction starts to drop significantly. This is because both are sensitive to the efficiency and timing of stellar feedback (Rosdahl et al. 2018) and likely to resolution as well (Ma et al. 2020).

A second feature in Fig. 8 is the drift of the production of LyC photons to more and more massive halos with decreasing redshift (the red curve moves right). At the highest redshift range of $z = 15 - 11$, almost all the LyC photons are emitted in halos with $M_{\text{vir}} \lesssim 3 \times 10^9 M_{\odot}$. Since f_{esc} is fairly flat at these low halo masses, the halos

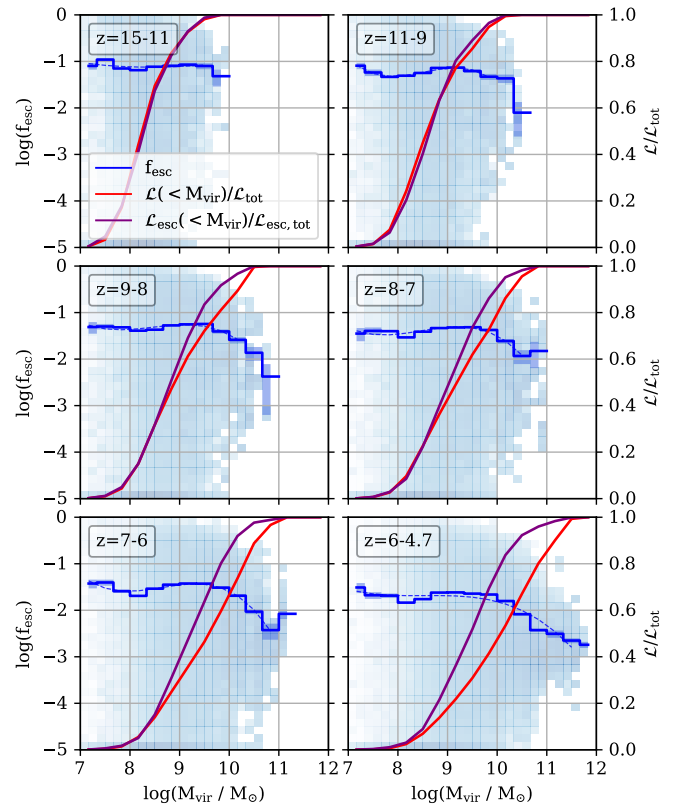


Figure 8. Intrinsic-LyC-luminosity-weighted mean escape fraction in SPHINX²⁰ versus halo mass (M_{vir}), in solid blue, stacked over snapshots with 5 Myr intervals at different redshift ranges, as indicated by legends in each panel. We also show the fraction of the total intrinsic (escaping) LyC luminosity emitted by halos with mass $< M_{\text{vir}}$, to be read against the right-side axis. To illustrate the scatter in f_{esc} for individual halos, we show in the background of each panel a 2D histogram of the normalised intrinsic LyC luminosity in bins of f_{esc} (floored at the lower y-limit) and halo mass, and the standard error of f_{esc} with a shaded region around the solid blue curve. The dashed blue curves show our best third-degree polynomial fits for $\log(f_{\text{esc}})$, which we describe in detail in Appendix D. At any given redshift, f_{esc} is fairly flat for $M_{\text{vir}} \lesssim 3 \times 10^9 M_{\odot}$, above which it decreases strongly with increasing halo mass. As seen by the red curve drifting towards more massive halos with decreasing redshift, the LyC photons are produced by increasingly massive halos, with decreasing f_{esc} , over time.

that produce LyC photons are also the ones from which LyC photons escape, and the red and purple curves are overlaid. As halos become more massive, the intrinsic luminosity drifts with decreasing redshift to higher masses. In the final redshift range of $z = 6 - 4.7$, LyC photons are predominantly emitted in massive halos, with only about 30% of them emitted in halos with $M_{\text{vir}} \lesssim 3 \times 10^9 M_{\odot}$. However, because of the shape of the f_{esc} versus M_{vir} relation, these low mass halos contributing to 30 percent of the intrinsic LyC emissivity still contribute to about 50 percent of the *escaping* emissivity, shown in purple.

3.5.2 Galaxy mass

We now look at f_{esc} versus galaxy stellar mass, M_* , in Fig. 9. At all redshifts we find a strong dependence of f_{esc} on M_* , with the highest f_{esc} found at intermediate masses of $\approx 10^7 M_{\odot}$ and declining f_{esc} for both increasing and decreasing M_* .

The drop in f_{esc} for $M_* \gtrsim 10^7 M_{\odot}$ is due to the decreasing effi-

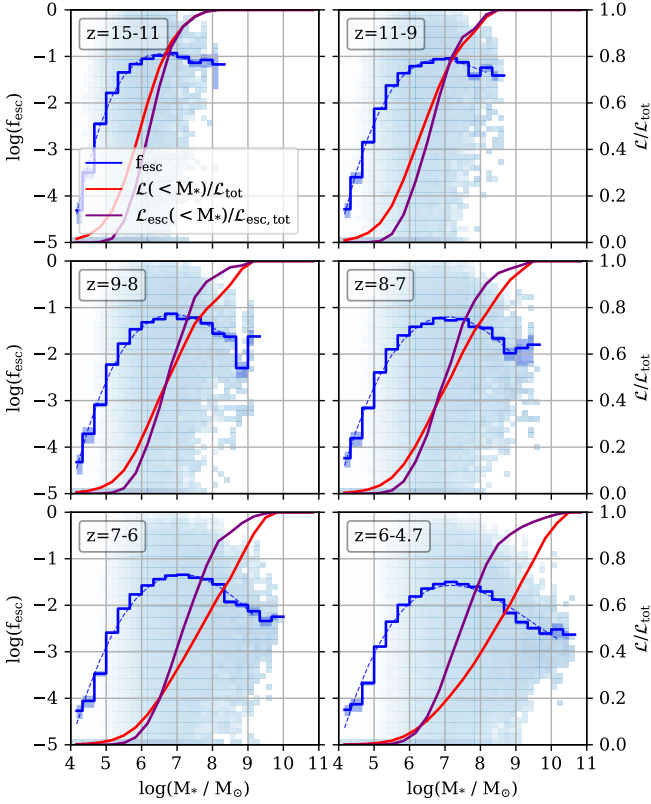


Figure 9. Correlation of intrinsic-luminosity-weighted mean escape fraction with galaxy stellar mass in SPHINX²⁰ at different redshifts. See the caption of Fig. 8 for a detailed explanation of the panels. At all redshifts, the escape fraction peaks at $M_* \approx 10^7 M_\odot$ and decreases for both lower and higher masses. As seen by the red curve drifting towards higher galaxy mass with redshift, LyC photons are produced in increasingly massive galaxies over time, which have decreasing f_{esc} .

ciency of stellar feedback with mass as already discussed and simply reflects the drop in f_{esc} for the parent halos with $M_{\text{vir}} \gtrsim 3 \times 10^9 M_\odot$ as seen in Fig. 8. The strong drop with f_{esc} towards the lowest galaxy masses, however, is more surprising and is not reflected in the f_{esc} versus halo mass relation. This drop appears to be due to star formation being unsustainable over time in the lowest-mass galaxies. For the more massive galaxies with $M_* \gtrsim 10^6 M_\odot$, star formation happens in bursts sustained over a few Myrs, leading to a) a collective burst of strong SN feedback and b) “support” by the SN feedback of the first stars born in clearing channels for LyC radiation to escape from successively formed ones. For the lowest-mass galaxies, however, the bursts are more discrete and less sustained, with typically one or very few stellar particles formed ($400 M_\odot$ in mass each), making their SN feedback less disruptive and weaker in facilitating the LyC radiation to escape. This is likely due to radiation feedback: as shown in e.g. Agertz et al. (2020); Smith et al. (2020), ionizing radiation feedback suppresses the clustering of star formation in low-mass galaxies, leading to a negative form of feedback where the efficiency of SN explosions is weakened. As low-mass galaxies grow, star formation becomes more clustered, whereby SN explosions become more efficient and increasingly the first stars born in a starburst can help clear away gas from their younger siblings, increasing the escape fraction.

At first glance, the correlation between f_{esc} and galaxy mass appears inconsistent with that for halo mass (Fig. 8), which does not show a decline in f_{esc} for the lowest halo masses. However, the

unvarying escape fraction for the lowest halo masses is just a consequence of the large scatter in the stellar mass to halo mass at those low masses, as seen in Fig. 4. For the lowest-mass halos, the mean escape fraction (which, we remind, is luminosity weighted) is dominated by the most luminous galaxies in the bin, which also have the highest stellar mass and the highest escape fractions. This leads to a fairly flat f_{esc} with halo mass.

A similar peak at a certain galaxy mass and turndown for both lower and higher galaxy masses was found by Ma et al. (2020), though their peak is at $M_* \approx 10^8 M_\odot$, about ten times higher than in our case. The reason for their peak being at a higher stellar mass is likely that their sub-grid (radiation and SN) stellar feedback is significantly more efficient in suppressing star formation than in SPHINX, leading to a stronger negative radiation feedback at low masses and stronger positive SN feedback at higher masses. As do we, Ma et al. (2020) find their escape fraction to be fairly insensitive to *halo* mass at the low-mass end, again likely due to the scatter in the stellar to halo mass at the low-mass end.

However, for these lowest-mass galaxies, we are in discord with other works using extreme-resolution simulations. Kimm et al. (2017) studied the escape of LyC radiation from mini-halos ($M_{\text{vir}} \sim 10^8 M_\odot$) in the EoR using cosmological RHD zoom simulations of extremely high resolution ($\Delta x_{\text{min}} \lesssim 1$ pc). They used the same code as we do in this paper and similar methods for star formation and feedback, but additionally included PopIII stars and molecular hydrogen formation. Contrary to the current paper, they found high (luminosity-weighted) mean escape fractions on the order of ≈ 40 percent for halos with $M_{\text{vir}} \lesssim 10^7$ and a significant drop in f_{esc} with increasing mass for $10^7 M_\odot \lesssim M_{\text{vir}} \lesssim 10^8 M_\odot$. Similar results were found, using a different code and methods but comparable resolution and physics, by Wise et al. (2014); Xu et al. (2016). These authors attribute these very high escape fractions in mini-halos to radiation feedback, i.e. the LyC radiation breaking itself out in these low-mass halos. Although this can in part be due to their inclusion of PopIII stars, which are very luminous, we find it likely that the lack of strong enough LyC feedback in low-mass SPHINX galaxies is a numerical limitation due to our finite resolution (≈ 10 pc versus ≈ 1 pc in Wise et al. 2014; Kimm et al. 2017). Presumably, higher resolution would produce high escape fractions in galaxies with $M_* \lesssim 10^5 M_\odot$, corresponding to the halo masses where escape fractions are high in the aforementioned works, and in accordance with those high-resolution results, the escape fractions would drop and converge with what we find for SN feedback regulation at $M_* \gtrsim 10^5 M_\odot$. Reassuringly, Kimm et al. (2017) find that these low mass halos with $M_{\text{vir}} \lesssim 10^8 M_\odot$ (or $M_* \lesssim 10^5 M_\odot$) contribute very little to reionization despite their high escape fractions, because they are very susceptible to feedback and hence are very dim. To summarise, the drop we see in f_{esc} for $M_* \lesssim 10^7 M_\odot$ is probably real, due to negative radiation feedback, but in reality the escape fraction rises again for $M_* \lesssim 10^5 M_\odot$ where radiation feedback can do serious damage.

We now consider the redshift-evolution of the fraction of intrinsic LyC luminosities of galaxies versus mass, shown in red in the panels of Fig. 9. At the highest redshift range of $z = 15 - 11$, about 90% of the LyC photons are coming from galaxies below the peak- f_{esc} mass of $10^7 M_\odot$. Since the escape fraction is rising with increasing galaxy mass in these galaxies, the escaping LyC luminosity, in purple, is shifted somewhat towards more massive galaxies compared to the intrinsic one. As galaxies become more massive, the intrinsic luminosity drifts to the right with decreasing redshift, and at the end of reionization (rightmost bottom panel), $\approx 80\%$ of the emitted LyC photons are coming from galaxies above the peak- f_{esc} mass (i.e. $M_* > 10^7 M_\odot$). Because of the shape of the f_{esc} versus galaxy mass

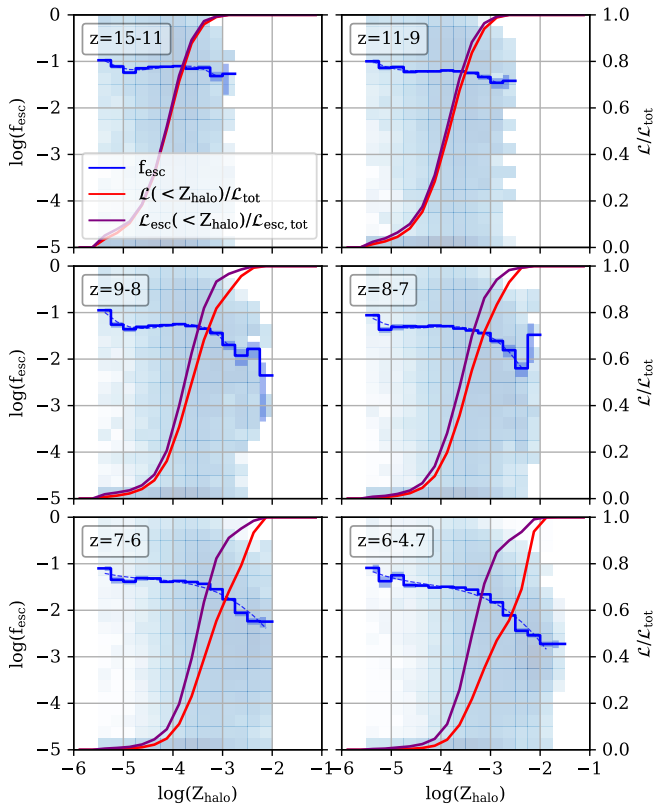


Figure 10. Correlation of intrinsic-luminosity-weighted mean escape fraction with luminosity-weighted metal mass fraction, Z_{halo} , in SPHINX²⁰ at different redshifts. See the caption of Fig. 8 for a detailed explanation of the panels. Galaxies with metallicities $Z_{\text{halo}} \gtrsim 3 \times 10^{-4}$ (more than about one percent Solar) tend to have low escape fractions, due to efficient cooling and because they are massive. The global LyC emissivity drifts with decreasing redshift towards more metal-rich galaxies, which have low f_{esc} .

relation, the escaping LyC emissivity is now shifted to lower galaxy masses compared to the intrinsic emissivity, with e.g. $M_* < 10^8 M_{\odot}$ galaxies accounting for $\approx 70\%$ of the escaping luminosity but only 40% of the intrinsic luminosity.

3.5.3 Metallicity

We examine f_{esc} versus LyC-luminosity-weighted stellar metallicities of galaxies, or Z_{halo} , in Fig. 10. We find a fairly flat escape fraction for $\sim 10^{-5} \lesssim Z_{\text{halo}} \lesssim 3 \times 10^{-4}$, a drop in f_{esc} for higher metallicities, and a spike in f_{esc} for the floor metallicity of $Z_{\text{halo}} = 6.4 \times 10^{-6}$. The decrease in f_{esc} with “high” metallicities has also been found by Yoo et al. (2020) and is due to enhanced cooling in metal-rich gas which weakens the efficiency of SN explosions in clearing away dense LyC-absorbing gas.

We note that we find more or less the same correlation and redshift evolution for *mass-weighted* stellar metallicities, which is less biased towards the youngest (and most luminous) stars in each galaxy.

A comparison of the different panels in Fig. 10 shows that LyC photons are produced in increasingly metal-rich galaxies with decreasing redshift (red curve drifting towards right with redshift). The drift for *escaping* radiation with redshift (purple curves), however, is slower, due to those metal-rich galaxies having very low escape fractions.

3.5.4 Specific star formation rate

Several works have argued that if the escape of LyC is regulated by feedback, it should be the highest in galaxies experiencing the strongest starbursts. Heckman et al. (2011) proposed that intense star formation, followed by extreme feedback, is a driver of high f_{esc} . Sharma et al. (2017) similarly argued that galaxies with high star formation rate surface densities have high f_{esc} , as these same galaxies are observed to be able to generate galactic winds, which should clear a way for LyC radiation escape. Faucher-Giguère (2020) took the argument a step further, suggesting that a decreasing intensity of star formation and, hence, feedback in the expanding Universe could drive the global escape fraction to decrease with cosmic time.

We therefore explore the correlation between f_{esc} and star formation in SPHINX. Using the star formation rate (SFR) of galaxies as a proxy for extreme star formation is not the best approach, since it is very biased towards the most massive galaxies. Instead we quantify the extremeness of star formation via the specific star formation rate, sSFR_{τ} , which is calculated for each galaxy as

$$\text{sSFR}_{\tau} = \frac{\text{SFR}_{\tau}}{M_*} = \frac{M_*(\text{age} < \tau)}{\tau M_*}, \quad (1)$$

where M_* is the stellar mass of the galaxy and τ is the lookback time, in Myr, over which we average the star formation rate (SFR). In other words, sSFR_{τ} is the ratio of the mass of stars formed in the previous τ Myrs versus the total stellar mass of the galaxy⁴. We consider specific star formation rates with two lookback times, short-term with sSFR_{10} and long-term with sSFR_{100} . The former roughly corresponds to star formation rates observationally determined via H α and the latter via FUV (e.g. Kennicutt & Evans 2012). By our Eq. (1) definition, sSFR_{10} can be in the range $[0, 100] \text{ Gyr}^{-1}$ and sSFR_{100} can be in the range $[0, 10] \text{ Gyr}^{-1}$, the upper limits meaning that all the stars in a galaxy have been formed in the last τ Myrs. Since sSFR_{10} is measured on a shorter timescale, it is a better indicator of the extremeness of star formation than sSFR_{100} , but is restricted to either ongoing or very recent starbursts. The longer-term sSFR_{100} can either indicate intense starbursts in the last 100 Myrs or alternatively a steady rate of star formation over the same period, and is hence not a perfect indicator of the most intense starbursts.

We show the correlation of f_{esc} with the shorter-term sSFR_{10} in Fig. 11 (blue curve) over six redshift intervals. At all redshift ranges except perhaps the earliest one, there is a strong increase in f_{esc} with sSFR_{10} for galaxies experiencing the strongest starbursts, with $\text{sSFR}_{10} \gtrsim 30 \text{ Gyr}^{-1}$. At lower sSFRs, we find f_{esc} reaching the lowest values at intermediate sSFRs and rising towards the lowest sSFRs. Comparing the red curves in each panel, we see an evolution in LyC photons being emitted from galaxies with decreasing sSFRs with decreasing redshift.

The peak in f_{esc} at the high sSFR_{10} -end fits the expectation that starbursts lead to high escape fractions. But what about the high escape fractions that we find for low sSFRs? Upon examination of randomly selected halos with low sSFR_{10} and high f_{esc} , we find that these are typically galaxies that have recently, *but not very recently* (i.e. more than $\tau = 10$ Myr), experienced starbursts and then subsequent feedback episodes that ejected nearly all the ISM gas. These violent ejections of gas have three effects: i) f_{esc} becomes high, because there is little gas remaining within the halo to absorb

⁴ Note that for simplicity we use the *initial* or formed stellar mass in both the numerator and denominator of Eq. (1), whereas it is more traditional to use the *current* mass (accounting for stellar mass loss) in the denominator.

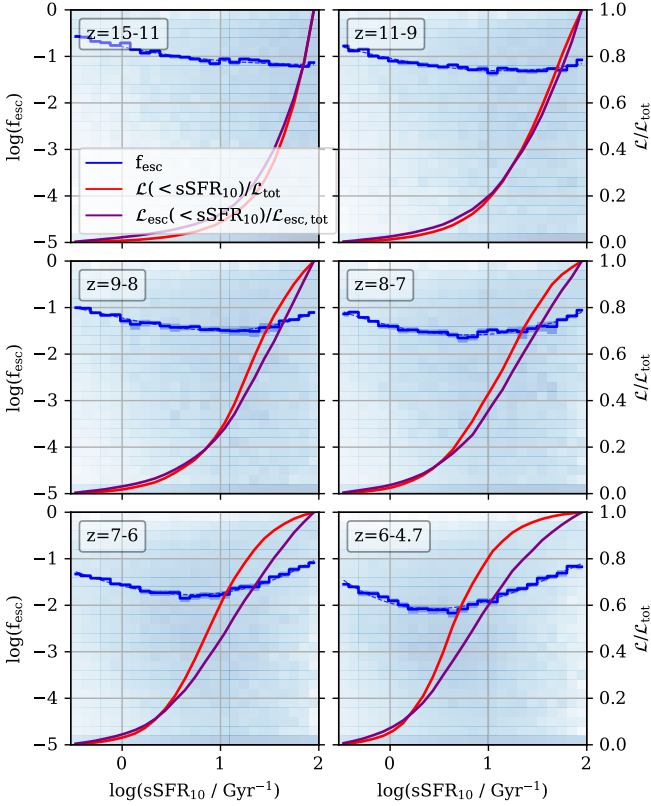


Figure 11. Correlation of intrinsic-luminosity-weighted mean escape fraction with short-term specific star formation rate, $sSFR_{10}$, in SPHINX²⁰ at different redshifts. See the caption of Fig. 8 for a detailed explanation of the panels. Note that we have floored galaxies with $sSFR_{10}$ below the range to the leftmost $sSFR_{10}$ bin, so they are counted in the plots. The galaxies experiencing the highest $sSFR_{10}$ have higher mean escape fractions than those with moderate $sSFR_{10}$. Galaxies with very low $sSFR_{10}$ also have high mean escape fractions, especially at high z , though they do not contribute much to the total LyC budget. The global LyC emissivity drifts significantly with decreasing redshift towards galaxies with decreasing $sSFR_{10}$.

the radiation, ii) the SFR becomes very low or even zero, because there is no longer any gas to fuel star formation, and iii) the LyC luminosity becomes very low because of effect ii). We have shown two examples of low-mass halos in this quenched, high f_{esc} state in the rightmost two panels in the bottom row of Fig. 2.

Both a very high and a very low $sSFR_{10}$ seems to be a good indicator of high f_{esc} , though the latter class of halos does not contribute very significantly to reionization (purple curves in Fig. 11). However, as is evident from the background 2D histograms in Fig. 11, there is huge scatter in f_{esc} at any $sSFR_{10}$, so spotting a galaxy with a very high (or very low) $sSFR_{10}$ is by no means a guarantee of spotting a high escape fraction.

We show in Fig. 12 the correlation of f_{esc} with the longer-term $sSFR_{100}$. As expected, the highest $sSFR_{100}$ galaxies have the highest escape fractions. However, the peak in f_{esc} is somewhat weaker than for high- $sSFR_{10}$ galaxies. This is because $sSFR_{100}$ is not as useful as $sSFR_{10}$ in singling out starbursts – a high $sSFR_{100}$ can mean anything between a quick intense starburst and a fairly robust but relatively continuous episode of star formation with low f_{esc} , lasting over tens of Myrs whereas the majority of LyC photons are produced within 10 Myrs from the starburst. As for $sSFR_{10}$, we see an evolution of LyC radiation being emitted from galaxies with decreasing $sSFR_{100}$

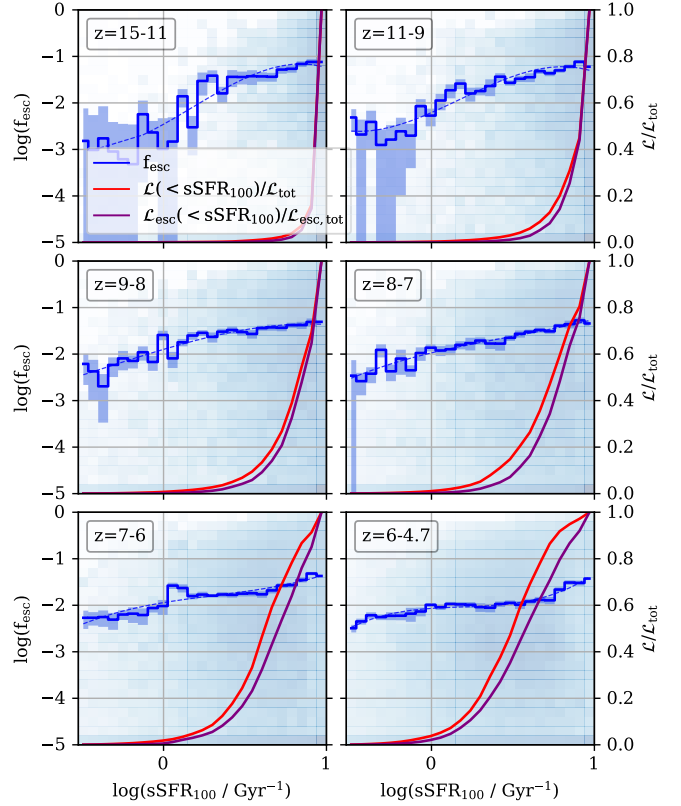


Figure 12. Correlation of intrinsic-luminosity-weighted mean f_{esc} with long-term specific star formation rate, $sSFR_{100}$, in SPHINX²⁰ at different redshifts. See caption of Fig. 8 for a detailed explanation of the panels. Note that we have floored galaxies with $sSFR_{100}$ below the range to the leftmost $sSFR_{100}$ bin, so they are counted in the plots. The correlation of f_{esc} with $sSFR_{100}$ is more straightforward than with $sSFR_{10}$, with overall decreasing f_{esc} for decreasing $sSFR_{100}$. Like for $sSFR_{10}$, the global LyC emissivity drifts significantly with time towards galaxies with decreasing $sSFR_{100}$.

with decreasing redshift. The lack of high f_{esc} for galaxies at the very low $sSFR_{100}$ -end further supports our interpretation that high f_{esc} for low shorter-term $sSFR_{10}$ in Fig. 11 indeed comes from highly disrupted galaxies that recently, but not too recently, experienced starbursts and then shut down star formation, hence having very low $sSFR_{10}$ but still moderate or high $sSFR_{100}$.

Correlations between f_{esc} and $sSFR$ has not been examined often in previous simulation works predicting escape fractions, but both Xu et al. (2016) with the Renaissance simulations, and Paardekooper et al. (2015) with the FiBY simulations, find high escape fractions for galaxies with the very highest short-term $sSFR_{10}$, with which we are in agreement.

Several works have suggested a positive correlation between f_{esc} and the SFR surface density Σ_{SFR} (e.g. Heckman 2000; Sharma et al. 2017; Naidu et al. 2019). Σ_{SFR} is a somewhat similar quantity to $sSFR$, the former being SFR per area and the latter per mass. We will analyse Σ_{SFR} and how it correlates with f_{esc} in SPHINX in a follow-up paper, as it adds too much to the scope of the present one.

3.5.5 UV magnitude

We finally consider in Fig. 13 the correlation of LyC escape fractions of galaxies with their 1500 Å UV magnitudes, or M_{1500} . We show here attenuated UV magnitudes, retrieved by Monte-Carlo ray-

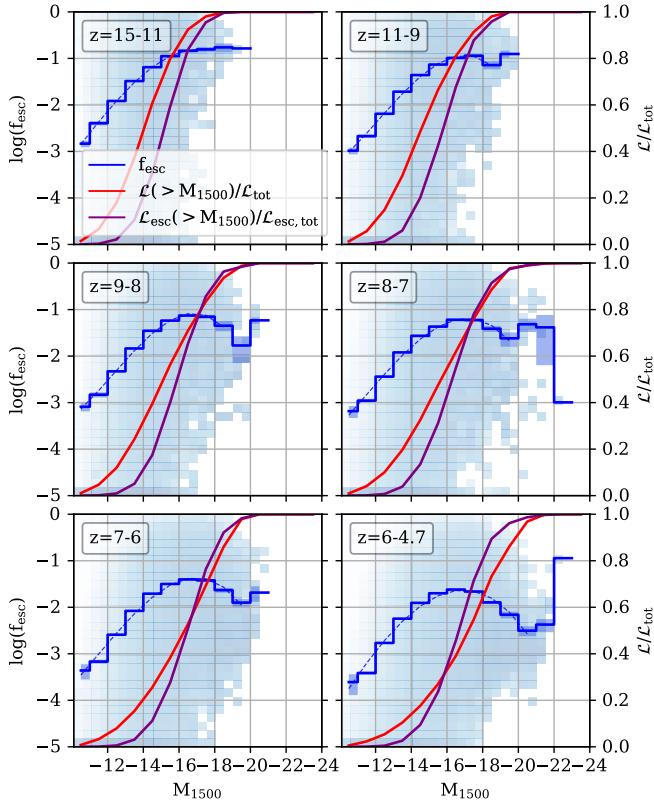


Figure 13. Correlation of intrinsic-luminosity-weighted mean escape fraction with 1500 Å magnitude (M_{1500}), in SPHINX²⁰ at different redshifts. See the caption of Fig. 8 for a detailed explanation of the panels. The correlation of f_{esc} with M_{1500} more or less mirrors that of galaxy stellar mass, except for a conspicuous peak in f_{esc} for the brightest galaxies, which is an attenuation effect.

tracing from the stellar particles and through the dusty ISM, as described in Section 2.2.

Ignoring the peaking f_{esc} for the very brightest galaxies seen in most panels of Fig. 13 (which we discuss in the next paragraph), we find a similar correlation of f_{esc} with M_{1500} as with M_* , with a peak at intermediate luminosities where SN feedback is most disruptive and a declining f_{esc} for both dimmer (less massive) and brighter (more massive) galaxies. We find an evolution with redshift of brighter galaxies dominating both the intrinsic and escaping LyC emission (red and purple curves, respectively).

The jump in escape fractions for the very brightest galaxies seen in most redshift ranges is due to the small statistics at the bright end as well as the tendency of the most attenuated galaxies at the bright end to have low escape fractions, often leaving at the very bright end one or a few galaxies that have small attenuation and high f_{esc} . This noise-effect would disappear with larger volume sizes, leaving a simple drop in f_{esc} with increasing brightness at the bright end.

3.6 Contributions to the ionizing radiation budget

We now assess in more detail how different galaxies in SPHINX²⁰ contribute to the escaping LyC budget during reionization. Fig. 14, taking inspiration from Hutter et al. (2020), shows these contributions for different halo properties in solid curves (and corresponding shaded regions). We calculate this contribution as the number of escaping LyC photons produced since the beginning of time for all

halos with a given property, divided by the total number of escaping photons that have been produced by all halos. To demonstrate the difference between the escape and production of LyC photons, we show in dotted curves the *intrinsic* fraction of LyC radiation produced, i.e. assuming unity escape fraction for all halos. Finally, for reference, the dashed curves show the reionization history in form of the volume-weighted neutral fraction, Q_{HI} .

The top left panel of Fig. 14 shows relative contributions to the LyC budget by halo mass. Due to the hierarchical nature of halo formation and growth of halos over time, increasingly massive halos dominate the intrinsic production of LyC photons with decreasing redshift. Because of the relatively low escape fractions of the most massive halos, this evolution is not as strong for the production of *escaping* LyC photons and the most massive halos, even if they intrinsically produce a lot of LyC photons, make a disproportionately small contribution to reionization. For example, halos with $M_{\text{vir}} \geq 10^{10} M_{\odot}$ are responsible for about 47 percent of all LyC photons produced by the end of reionization (dotted red curve), but they account for slightly less than 20 percent of the *escaping* LyC photons. Looking at galaxy masses (top right panel), we find a similar evolution in the intrinsic LyC production (dotted curves) towards increasingly massive galaxies with time. As galaxies in the mass range $10^8 M_{\odot} > M_* > 10^6 M_{\odot}$ have the highest mean escape fractions, this mass range dominates the production of escaping LyC radiation by the end of reionization, being responsible for about 70 percent of the escaping budget but only 40 percent of the intrinsic one. This translates similarly to UV magnitude, shown in the middle left panel. Intermediate-brightness halos with M_{1500} in the range $[-14, -18]$ are responsible for ≈ 75 percent of the escaping LyC photons by the end of reionization, while intrinsically producing only ≈ 50 of the budget.

Taking sensitivity limits of current EoR surveys at $M_{1500} \approx -17$, where discrepancies in the UV luminosity function between different works become larger than order-of-magnitude at $z \lesssim 6$ (Bouwens et al. 2017), we can estimate from the middle left panel in Fig. 14 that the constrained part of the high- z luminosity function contains galaxies responsible for about 45 (52) percent of the LyC photons emitted into the IGM (produced in the ISM) up to the end of reionization. Upcoming James Webb Space Telescope (JWST) surveys will have a sensitivity limit of $M_{1500} \approx -16$ for $z \approx 7$ (see Hutter et al. 2020), so they should, according to the same plot, capture galaxies responsible for about 68 percent of the LyC photons contributing to reionization.

LyC photons are produced by increasingly metal-rich halos over time as seen in the middle right panel of Fig. 14. The escaping LyC budget is shifted from the intrinsic one towards metal-poor halos, which have higher escape fractions. Relatively metal-rich halos with $Z_{\text{halo}} \geq 10^{-3}$ intrinsically produce slightly more than 50 percent of all LyC photons by the end of reionization, but since their escape fractions are low, they are responsible for only ≈ 17 percent of the *escaping* photons.

Finally, in the bottom panels, we see clearly a drift in the intrinsic production of LyC radiation with time towards galaxies with lower specific star formation rates, i.e. less intense star formation. Since halos with more intense star formation tend to have higher escape fractions, this evolution is not as strong in the sense of escaping LyC production.

3.6.1 Comparison with literature

Katz et al. (2018) used a SPHINX-like simulation to study the contributions of halos in different mass ranges to reionization, using the same code and in most respects similar methods as us, but a smaller

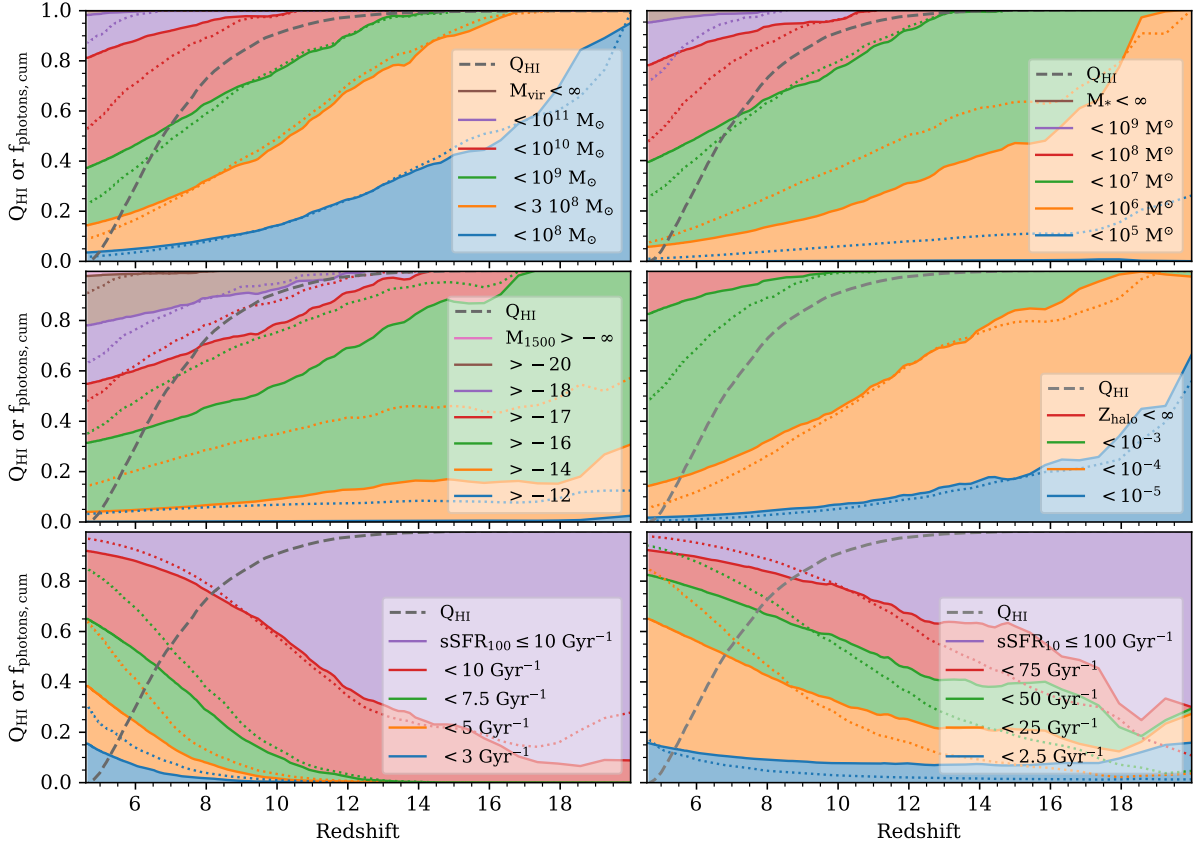


Figure 14. Each panel shows the cumulative relative contributions of halos in SPHINX^{20} to the total number of LyC photons escaping into the IGM (emitted from stars) in solid (dotted) curves, and for reference we also show the redshift evolution of the volume-weighted neutral fraction in dashed curves. Colors indicate halo properties as described in the legend of each panel. Shaded regions describe bins in halo properties, for escaping luminosities only. Clockwise from top left, the plots show contributions of halos with different M_{vir} , M_* , LyC-luminosity-weighted stellar metallicity, sSFR_{10} , sSFR_{100} , and dust-attenuated UV magnitudes. Both the intrinsic and escaping production of LyC photons drift over time towards increasingly massive halos containing galaxies with increasing mass, metallicity, and brightness, and decreasing sSFR .

volume (10 cMpc wide), lower resolution (25 times more massive DM particles and 12 times wider ISM cells), and the older BPASS SED version that we use in $\text{SPHINX}^{10}_{\text{early}}$. Their halo contributions to reionization are fairly similar to both SPHINX^{20} and $\text{SPHINX}^{10}_{\text{early}}$ (see Appendix B) in terms of halo mass. Their $M_{\text{vir}} < 10^9$ and $< 10^{10} M_{\odot}$ halos produce ≈ 20 and ≈ 70 percent of the LyC photons reionizing the IGM, respectively, while our corresponding numbers are ≈ 37 and ≈ 80 percent. “Intermediate” mass halos of $M_{\text{vir}} = 10^9 - 10^{10} M_{\odot}$ are hence significantly more dominant than in SPHINX^{20} at the cost of lower-mass halos which are not represented in Katz et al. (2018) due to lower resolution. Using the CoDa II large-volume (100^3 cMpc 3) simulations, Lewis et al. (2020) found similar halo contributions to Katz et al. (2018), with $M_{\text{vir}} < 10^9$ and $< 10^{10} M_{\odot}$ halos producing ≈ 20 and ≈ 80 percent of the LyC photons escaping into the IGM at $z = 7$, when their volume is 50 percent reionized. Here the somewhat stronger contribution of massive halos compared to SPHINX is not due to the DM resolution, which is similar to SPHINX . Instead, it is likely due to the lower physical resolution, Lewis et al. (2020) having a co-moving uniform cell width of 23 kpc or 3.3 kpc at $z = 6$ (300 times wider than in SPHINX), leading to little star formation in low-mass halos. Yet it is quite remarkable that these three suites of simulations find fairly similar contributions of halo masses to reionization despite their large differences in resolution and volume size.

Hutter et al. (2020) studied how four different semi-analytic models

affect reionization, and specifically investigated contributions from halos with different masses to reionization as in our top left panel in Fig. 14. Their model that agrees best with our halo-mass contribution to reionization is “early heating” which assumes a halo mass-dependent escape fraction, decreasing with halo mass. Their other models assume fixed escape fractions and have significantly larger contribution from massive and UV-bright halos than SPHINX . This is not surprising, since the “early heating” assumption matches qualitatively the f_{esc} to halo mass correlation found in SPHINX , as well as Lewis et al. (2020) and several other simulation works. However, the “early heating” model in Hutter et al. (2020) has reionization being predominantly driven by very dim galaxies with $M_{1500} \gtrsim -14$. This is far from what we find in the middle left panel in Fig. 14, so the scenario is not fully compatible with SPHINX . The reason for the discrepancy is that low-mass halos in Hutter et al. (2020) are assumed to have much higher escape fractions ($f_{\text{esc}} \approx 60\%$ for $M_{\text{vir}} \leq 10^9 M_{\odot}$) than we find in SPHINX .

Similarly, Finkelstein et al. (2019) conclude, using the well-known differential equation from Madau et al. (1999) describing the competition of photo-ionization and recombination of the IGM, that reionization is predominantly driven by significantly dimmer galaxies than in SPHINX , or with $M_{1500} > -15$. Here again the discrepancy is likely mostly due to differences in escape fractions for low-mass galaxies. They assume escape fractions, taken from the cosmological simula-

tions of [Paardekooper et al. \(2015\)](#), that are strongly dependent on halo mass, being fairly high for very low-mass halos and essentially zero for $M_{\text{vir}} \gtrsim 10^9 M_{\odot}$, i.e. their escape fraction drops with increasing mass as in SPHINX but starts dropping at much lower masses. We can only guess at the reason for this difference between [Paardekooper et al. \(2015\)](#) and SPHINX: it could be due to their use of the non-binary Starburst99 SED model, too-late or inefficient SN feedback, or their lack of massive halos.

[Naidu et al. \(2019\)](#), using a semi-analytic model, argue that reionization is driven primarily by the most massive ‘‘Oligarch’’ galaxies, with $M_{\text{vir}} \gtrsim 10^{10} M_{\odot}$ halos responsible for about 95 percent of the LyC photons reionizing the IGM. This result is in strong contrast with SPHINX and rests on two assumptions: a positive correlation $f_{\text{esc}} \propto \Sigma_{\text{SFR}}^{0.4}$ between the escape fraction and SFR surface density and a positive correlation between halo mass and Σ_{SFR} . Together, these assumptions lead to a positive correlation between f_{esc} and halo mass, i.e. the most massive halos get the highest f_{esc} , which is contrary to SPHINX and almost all other galaxy formation simulations predicting f_{esc} . Therefore, either of the assumptions must hold false in SPHINX in order for the most massive halos to have the lowest escape fractions. Assessing this is beyond the scope of the current paper but we will study Σ_{SFR} in SPHINX and how it correlates with both f_{esc} and halo mass in a follow-up paper.

3.7 What regulates the global escape fraction?

In Fig. 6 we have seen that the global LyC escape fraction from galaxies decreases significantly with decreasing redshift. Theoretical models of reionization and for the redshift evolution of the intergalactic UV background (e.g. [Haardt & Madau 2012](#); [Khaire & Srianand 2018](#); [Puchwein et al. 2019](#); [Faucher-Giguère 2020](#)) require qualitatively the same evolution of the global escape fraction in order to produce a sufficient amount of ionizing radiation in the IGM during the EoR, to not produce an overly strong low- z UV background, and match the general observational constraint of low escape fractions at low redshift (e.g. [Matthee et al. 2016](#); [Grazian et al. 2017](#); [Rutkowski et al. 2017](#)). Those theoretical models vary significantly in the exact form of the assumed evolution of the global f_{esc} with redshift, but the general trend is always there and is qualitatively similar to the evolution of f_{esc} that naturally comes out of the SPHINX simulations, as we show by including in Fig. 6 the escape fraction evolution in [Haardt & Madau \(2012\)](#) and [Faucher-Giguère \(2020\)](#). Therefore, SPHINX not only confirms such an evolution but also provides an opportunity to investigate what drives it.

We have already seen in Figures 8-12 that LyC-weighted mean escape fractions for individual galaxies in SPHINX decrease with increasing halo mass, increasing galaxy mass, increasing metallicity, and decreasing sSFR (except for the turn-over at very low sSFR₁₀). The same figures also show, with red curves, that with decreasing redshift the intrinsic production of LyC radiation is increasingly dominated by these massive, metal-rich, and mildly star-forming galaxies which have low f_{esc} , i.e. the red curve slides to the right with decreasing redshift for M_{vir} , M_* , and Z_{halo} , and to the left for sSFR₁₀. Therefore it seems plausible that the decrease of the global f_{esc} with redshift is dictated by this shift of intrinsic LyC production to galaxies with low f_{esc} .

Yet, the very same figures also suggest that none of those factors alone (i.e. mass, metallicity, or sSFR) regulates the decreasing f_{esc} . Taking for example Fig. 8 showing the correlation of f_{esc} with halo mass, a comparison of the different panels reveals that f_{esc} decreases with redshift for any fixed M_{vir} . *If the mass evolution predominantly drove the decrease in f_{esc} with redshift, f_{esc} would remain fixed*

with redshift for any fixed M_{vir} , and this is clearly not the case. Hence there must be some other factor than just halo mass evolution significantly contributing to the decrease of the global f_{esc} with time. The same is true for all the halo properties explored in Figures 8-13, i.e. f_{esc} decreases with decreasing redshift for any fixed galaxy mass, metallicity, sSFR, and magnitude.

It is possible that two or several factors regulate the escape fraction together, e.g. an increase in mean metallicity causing a drop in f_{esc} for a fixed stellar mass and similarly an increase in mean stellar mass causing a drop in f_{esc} for a fixed metallicity. However, we find from two-dimensional histograms, i.e. plotting escape fractions against two halo properties together (not shown), that this is not the case for any two properties from Figures 8-13 combined.

However, even if we do not find a drop in f_{esc} with redshift for fixed sSFR, this does not close the case on the possibility that a decreasing intensity of star formation in the Universe with redshift, and hence a decrease in the intensity of stellar feedback, drives a decrease in LyC escape fractions from galaxies. As touched upon in §3.5.4, the flaw in sSFR₁₀ is that it does not capture the long-term effect of starbursts and the ensuing feedback that can last tens of Myrs. When a galaxy is severely disrupted by stellar feedback and its f_{esc} becomes high, it can remain high for a long time while sSFR₁₀ becomes very low, since the gas fuelling star formation has been largely ejected. Therefore, sSFR₁₀ does not capture galaxies that have high f_{esc} and remaining non-negligible LyC luminosities, due to recent but quenched starbursts. These galaxies quickly become LyC-dim so most of them do not weigh very much in (the LyC-luminosity-weighted) f_{esc} , but some of them indeed do for a short time. sSFR₁₀₀ is a more long-term measure of the specific star formation rate, but this is also not a good measure as it does not discriminate efficiently between starbursts (with high f_{esc}) and steady but fairly high rates of star formation (with low f_{esc}).

As a more useful measure of current *and recent* star formation activity, we therefore take for each halo its maximum sSFR₁₀ over the last 50 Myrs. We calculate this in the following way for each halo: in a given simulation snapshot, we take all the stars in the halo and compute

$$\text{sSFR}_{10,\text{max}} = \max \left(\frac{\frac{M_*(X \leq \text{age} < X+10 \text{ Myr})}{10 \text{ Myr}}}{M_*(\text{age} \geq X)} \right), \quad (2)$$

for X in (0, 1, 2, ..., 50) Myr.

The 50 Myr lookback time is arbitrary and the results that follow are insensitive to it as long as it is significantly larger than 10 Myrs and $\lesssim 100$ Myrs.

We show in Fig. 15 how f_{esc} correlates with sSFR_{10,max} in the usual six redshift ranges. We find a quite different correlation here than with sSFR₁₀, shown in Fig. 11. For the high-sSFR end, the two correlations are fairly similar, but they are very different for sSFR₁₀ $\lesssim 10 \text{ Gyr}^{-1}$, with a fairly flat and low $f_{\text{esc}} \approx 0.01$ in the case of sSFR_{10,max} whereas there is a rise in f_{esc} for the lowest-sSFR₁₀ halos. The reason for this is that sSFR_{10,max} keeps memory of recent starbursts with high f_{esc} , i.e. a galaxy that recently experienced a starburst and is quenched but still exhibits a high f_{esc} will typically have a high sSFR_{10,max} but low sSFR₁₀. Another striking difference between the correlations of f_{esc} with sSFR₁₀ on one hand and sSFR_{10,max} on the other is that in the latter case there is much less evolution of the correlation with redshift. For any fixed sSFR_{10,max} and especially for sSFR_{10,max} $\gtrsim 10 \text{ Gyr}^{-1}$, the escape fraction does not drop significantly with redshift. Furthermore we do see in Fig. 15, with the sliding red curve towards the left from

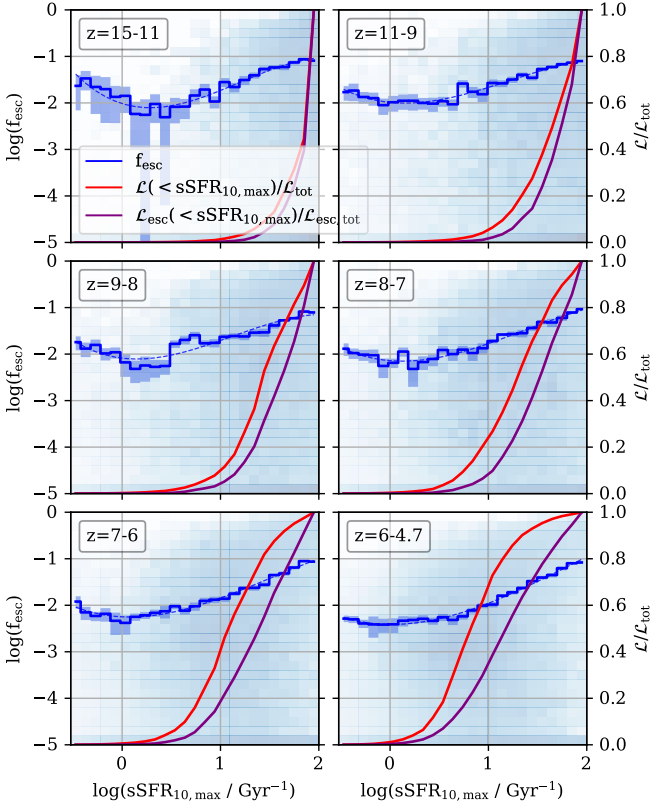


Figure 15. Correlation of intrinsic-LyC-luminosity weighted f_{esc} with $\text{sSFR}_{10,\text{max}}$, the maximum sSFR_{10} in the last 50 Myrs, in SPHINX²⁰ at different redshift ranges. See the caption of Fig. 8 for a detailed explanation of the panels. Note that we have floored galaxies with $\text{sSFR}_{10,\text{max}}$ below the range to the leftmost $\text{sSFR}_{10,\text{max}}$ bin, so they are counted in the plots. The correlation of f_{esc} is more monotonous here than with the *current* sSFR_{10} , shown in Fig. 11 and the correlation also varies much less with redshift.

high to low redshift, that LyC photons are produced in galaxies with decreasing $\text{sSFR}_{10,\text{max}}$ with decreasing redshift.

It therefore seems plausible that an evolving $\text{sSFR}_{10,\text{max}}$ with redshift is a driver of the decreasing global f_{esc} . To confirm that this is the case we examine in Fig. 16 the redshift-evolution of the luminosity-weighted mean f_{esc} for halos in bins of fixed $\text{sSFR}_{10,\text{max}}$. The idea is that if the global f_{esc} is regulated by an evolving $\text{sSFR}_{10,\text{max}}$, it should not vary with redshift when $\text{sSFR}_{10,\text{max}}$ is fixed, while the relative contribution to the total LyC emission should change and halos with low $\text{sSFR}_{10,\text{max}}$, corresponding to low f_{esc} , should increasingly dominate the intrinsic production of LyC photons. For each bin in $\text{sSFR}_{10,\text{max}}$, as indicated in the legend, a solid curve shows the LyC-luminosity-weighted mean escape fraction in SPHINX²⁰ averaged over 100 Myrs, $f_{\text{esc},100}$ ⁵, as a function of redshift, for all halos in a given $\text{sSFR}_{10,\text{max}}$ range, and a corresponding shaded region shows the fraction of intrinsically emitted LyC photons for the same halos.

We indeed find that a fixed burstiness, measured with $\text{sSFR}_{10,\text{max}}$, yields a fairly non-evolving mean f_{esc} . The figure therefore shows that the evolution in the global f_{esc} of LyC radiation from all galaxies (black thick curve) is mostly driven by the LyC radiation being

⁵ We prefer to average the escape fraction over time here rather than show the instantaneous f_{esc} , to reduce the noise, which increases when we narrow the set of halos included in the analysis by fixing halo properties.

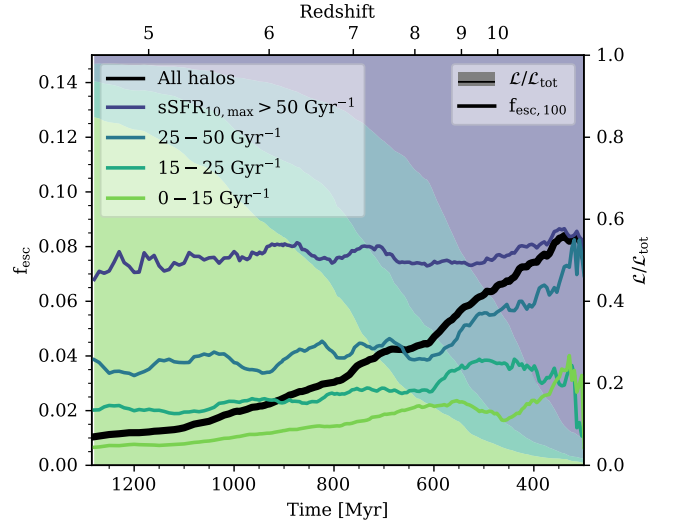


Figure 16. Global escape fraction averaged over 100 Myrs ($f_{\text{esc},100}$) versus redshift, in solid curves, for all halos in SPHINX²⁰ (thick black curve) and at fixed bins in $\text{sSFR}_{10,\text{max}}$ (thinner coloured curves). The shaded regions indicate the fractions of the total LyC radiation intrinsically produced by halos in these fixed $\text{sSFR}_{10,\text{max}}$ bins, and show that the LyC emission is dominated by decreasing $\text{sSFR}_{10,\text{max}}$ with decreasing redshift. For any fixed $\text{sSFR}_{10,\text{max}}$, halos have a fairly constant escape fraction. We conclude that the global decrease in f_{esc} with redshift is due to a decreasing efficiency of star formation in the Universe.

emitted from decreasingly bursty galaxies (i.e. going from dark blue to light green). There is significant noise in the curves, especially at $z \gtrsim 8$ for the bins with lower $\text{sSFR}_{10,\text{max}}$ and at lower redshift for the bins with higher $\text{sSFR}_{10,\text{max}}$, due to small numbers of halos populating those $\text{sSFR}_{10,\text{max}}$ -redshift combinations. For the lower redshifts shown, there is some evolution of the escape fraction for the lowest $\text{sSFR}_{10,\text{max}}$ -bin, decreasing by more than 50% from $z = 9$ to $z = 5$. This may be partly driven by the LyC radiation being produced by galaxies with increasing masses or metallicities, but it is probably predominantly an artificial effect of decreasing physical resolution with redshift, as we will discuss in §4.3.

We conclude from this analysis that the redshift-evolution of the global f_{esc} is driven mostly by an increasing fraction of galaxies with low $\text{sSFR}_{10,\text{max}}$ over time. Fig. 17 shows clearly that $\text{sSFR}_{10,\text{max}}$ decreases globally with decreasing redshift, whether computed as the median of all halos or the intrinsic LyC-luminosity weighted mean. To demonstrate that this evolution does not simply reflect the general evolution towards increasingly massive galaxies, for which extreme specific star formation rates cannot be maintained, we also show the evolution of $\text{sSFR}_{10,\text{max}}$ for a fixed range of stellar mass, roughly corresponding to the peak in f_{esc} seen in Fig. 9. For these fixed galaxy masses, $\text{sSFR}_{10,\text{max}}$ also drops with redshift. The decrease in $\text{sSFR}_{10,\text{max}}$ is thus not simply due to galaxies becoming more massive, but is rather due to less dense environments, less frequent mergers, and subsiding gas accretion (e.g. Dekel et al. 2009; Fakhouri et al. 2010; Tillson et al. 2011). This evolution, with or without fixed galaxy mass, is also true for sSFR_{10} and sSFR_{100} (not shown). Such an evolution of sSFR is plausible and found, at least qualitatively, by many observational and theoretical works (Lehnert et al. 2015; Fernández et al. 2018; Stefanon et al. 2021b, and references therein).

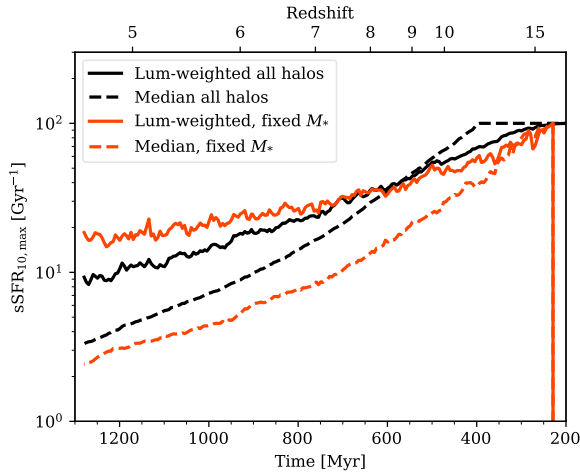


Figure 17. Redshift evolution of $s\text{SFR}_{10,\text{max}}$ in SPHINX^{20} . The dashed black curve shows the median $s\text{SFR}_{10,\text{max}}$ for all halos containing stars, while the solid black curve shows the intrinsic-LyC-luminosity-weighted mean for the same halos, showing better the evolution in $s\text{SFR}_{10,\text{max}}$ for LyC-emitting galaxies. The dashed and solid red curves show the same, but for the subset of halos that at each given redshift are in the stellar mass range $3 \times 10^6 M_{\odot} < M_* < 3 \times 10^7 M_{\odot}$. Even for a fixed galaxy mass, the specific star formation rate decreases significantly with redshift.

4 DISCUSSION

4.1 On the sensitivity of escape fractions to the SED model

We now briefly address why escape fractions (Fig. 6), and hence reionization (Fig. 5), are so sensitive to rather subtle variations in the SED model used. Fig. 18 shows escape fractions and cumulative LyC luminosities binned by stellar particle age in our two 10 cMpc SPHINX volumes, stacked over 34 snapshots in the redshift range $z = 7 - 6$. The fiducial BPASS version 2.2.1 (SPHINX^{10}) is shown in solid curves and the older version 2.0 ($\text{SPHINX}_{\text{early}}^{10}$) in dashed curves. The blue curves show the mean escape fraction as a function of age and demonstrate clearly how sensitive the escape fraction is to stellar age. With both BPASS versions, the escape fraction is very low for new-born stellar populations. Between ≈ 3 and 10 Myrs the escape fraction rises very steeply with age and reaches a peak. As several authors before us (e.g. Kimm & Cen 2014; Ma et al. 2016; Trebitsch et al. 2017), we interpret this sensitivity of f_{esc} to stellar age to be due to regulation by SN feedback: at age 3 Myrs, stellar particles start undergoing SN explosions, dispersing surrounding gas and clearing way for the radiation to escape from the exploding particles as well as their neighbouring particles. The escape fraction drops again beyond an age of 50 Myrs, which is the time at which stellar particles cease undergoing SN explosions. The escape fraction then stabilises at ~ 10 percent, with the old stellar particles scattered over the ISM and not especially correlated with the cold and neutral gas which most efficiently absorbs their LyC radiation.

The overall LyC-luminosity-weighted escape fraction for all stellar ages, indicated by horizontal lines in the left side of the plot, is about 60 percent higher in $\text{SPHINX}_{\text{early}}^{10}$ than in SPHINX^{10} . We attribute this difference to a combination of timing and the overall emission of LyC photons. The former is seen by comparing the solid and dashed red curves, which show the fraction of total intrinsic LyC emissivity below a given age. This is shifted towards higher ages with BPASS 2.0, as this model has significantly higher LyC luminosities at old ages compared to BPASS 2.2.1. Stellar populations older than 10 Myrs,

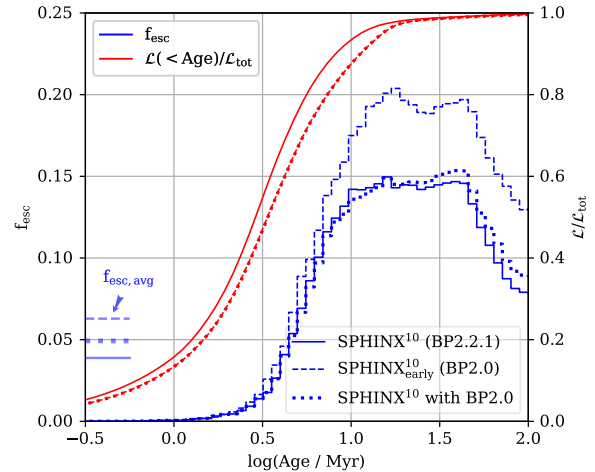


Figure 18. Escape fractions versus stellar particle age for all 34 snapshots between redshifts 7 and 6 in the 10 cMpc volumes with BPASS 2.2.1 (solid) and with BPASS 2.0 (dashed). Blue curves show the LyC-luminosity-weighted mean f_{esc} as a function of stellar age. Red curves show the fraction of total intrinsic LyC emissivity for all stellar particles younger than the given age. Dotted curves show results for the SPHINX^{10} simulation post-processed with the BPASS 2.0 model from $\text{SPHINX}_{\text{early}}^{10}$. Horizontal lines on the left side of the plot show the global f_{esc} for the three cases. The higher overall f_{esc} in $\text{SPHINX}_{\text{early}}^{10}$ compared to SPHINX^{10} is roughly equally due to the shift of the cumulative luminosity to older ages (i.e. effect of timing, isolated in the dotted curves) and the overall higher stellar luminosities (i.e. photo-ionization feedback).

with high escape fractions, emit about 10 percent of the intrinsic LyC radiation with the older BPASS model, but only about 5 percent of it with the newer model. Since the escape fraction is so sensitive to stellar age – which we remind is due to SN feedback – the small shift in the intrinsic emissivity with age leads to a significant difference in the overall escape fraction. The second effect, which is due to overall LyC luminosities rather than timing, is clear from the difference in the escape fraction versus age for the two SED models, i.e. the solid and dashed blue curves. For a given stellar population age, f_{esc} is consistently higher with BPASS 2.0 than with BPASS 2.2.1, by about 30 percent for age > 10 Myrs. The two simulations shown here are identical in setup except for the LyC luminosities of the stellar particles as a function of their age and metallicity, and we stress that the timing and energy release by SN explosions is on average the same in both simulations. We are therefore forced to conclude that *radiation feedback* provides an additional regulation of escape fractions, by ionising gas and slowly dispersing it away from stars. This happens more efficiently with BPASS 2.0, which produces about 30 percent more LyC photons per unit stellar mass for metal-poor stellar populations than version 2.2.1 (see Fig. 1).

The overall higher escape fractions with BPASS 2.0 are due both to timing – i.e. a larger fraction of LyC radiation remaining to be emitted at the onset of SNe as well – and the larger number of LyC photons emitted overall. The former effect has already been pointed out by Ma et al. (2016); Rosdahl et al. (2018), but the latter has largely been ignored. To distinguish their importance, we separate the two effects in the dotted curves in Fig. 18. Here we have post-processed the SPHINX^{10} simulation outputs with the older BPASS 2.0 model, i.e. we compute escape fractions in the BPASS 2.2.1 simulation assuming BPASS 2.0. This isolates the timing effect from that of radiation feedback, since the timing is changed from the

newer BPASS version but not the feedback. As expected, the escape fraction versus age (blue) is close to that of the SPHINX¹⁰ simulation with BPASS 2.2.1 while the cumulative intrinsic LyC luminosity (red) is almost identical to the SPHINX¹⁰_{early} simulation with BPASS 2.0. The global escape fraction from this experiment is shown in the horizontal dotted curve on the left side. It sits right between the two previous escape fractions, though slightly closer to that for SPHINX¹⁰ (solid). From this we conclude that timing and radiation feedback each contribute similarly to boosting the LyC escape fraction with the increased and delayed LyC luminosities in BPASS 2.0, with perhaps a slightly stronger effect from radiation feedback. This highlights the need for self-consistent RHD simulations to correctly predict escape fractions. Simply post-processing a non-RHD simulation, or post-processing an RHD simulation with an SED model different from the on-the-fly one, will yield inconsistent and wrong LyC escape fractions.

4.2 Convergence of results with volume size and SED model

Due to its large volume, we have focused our analysis on the SPHINX²⁰ simulation, despite the late reionization history it produces. We have verified that the general trends and conclusions on the dependence of escape fractions on galaxy properties, contributions of galaxies to reionization, and evolution of escape fractions with redshift hold for the smaller volume and brighter SED model. For reference we present this analysis in Appendix B. To summarise, the higher global escape fraction in the smaller volume SPHINX¹⁰ simulation is mostly due to the cut-off in the halo mass function being at lower mass than in SPHINX²⁰. Since SPHINX²⁰ has more of those massive halos, which we have shown to have low f_{esc} , its global escape fraction is lower than in the smaller volumes. However, we do also see a hint of escape fractions being generally lower for galaxies of all masses, metallicities, and magnitudes in SPHINX¹⁰ than in SPHINX²⁰. This can be due to cosmic variance or even simply noise, but it is possible that environmental effects play a minor role, i.e. less massive environments may have slightly higher escape fractions. This effect is out of the scope of the current paper and will be explored in future work. Since the SPHINX¹⁰ simulation is shifted to lower halo masses than SPHINX²⁰, the halo contributions to the LyC luminosity budget during reionization is very similar in the two simulations, except it is more noisy in SPHINX¹⁰ and slightly shifted to less massive, dimmer, and more metal-poor galaxies, whereas the contributions in terms of sSFR is almost identical between the two.

The only difference between SPHINX¹⁰ and SPHINX¹⁰_{early} is the assumed BPASS version, so we can safely conclude that the significantly higher global escape fraction in the latter is purely due to the different SED model. The comparison in Appendix B reveals much the same correlations of f_{esc} with halo properties in the two simulations, the f_{esc} curve simply being monotonously shifted up for SPHINX¹⁰_{early} compared to that of SPHINX¹⁰, though perhaps slightly increasingly with halo mass. Between SPHINX¹⁰ and SPHINX¹⁰_{early}, the halo contributions to the intrinsically emitted LyC radiation are very similar, while the escaping contributions are slightly shifted towards more massive and metal-rich halos.

Our trends of f_{esc} with halo properties and contributions of halos to reionization are therefore insensitive to variations in volume size and assumed SED model. We furthermore demonstrate in Appendix B that although the data are very noisy in the SPHINX¹⁰_{early} simulation due to the smaller volume, the global evolution in f_{esc} is driven there by a decreasing sSFR_{10,max}, as in SPHINX²⁰. Hence all our conclusions hold for reionization histories that bracket main-stream

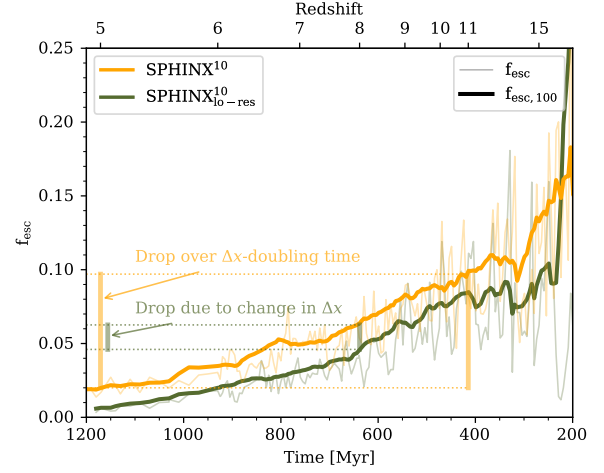


Figure 19. Global escape fraction with fiducial and degraded physical resolution (twice the minimum cell width), in yellow and green curves, respectively. Thin transparent curves show the instantaneous f_{esc} while thick curves show sliding luminosity-weighted averages over the previous 100 Myrs. Escape fractions are not converged with resolution, with lower resolution giving lower f_{esc} . The decrease in the global f_{esc} with redshift is therefore partly due to decreasing resolution, since the cell width Δx_{min} decreases linearly with the expansion factor in our constant co-moving resolution. However, the drop due to the evolving Δx_{min} is sub-dominant, as indicated by the relative sizes of the yellow and green vertical bars, which indicate the total drop in f_{esc} over the time it takes for the physical Δx_{min} to double and the drop in f_{esc} due to directly doubling Δx_{min} , respectively.

theoretical and observational constraints of reionization, from late in SPHINX²⁰ ($z = 4.64$) to early in SPHINX¹⁰_{early} ($z = 6.5$).

4.3 Resolution convergence

We finally investigate the convergence of our main results with resolution. We focus on the simulation cell width, Δx , which directly affects the porosity of the ISM through which LyC radiation propagates and therefore can be expected to affect LyC escape fractions. We recall that our minimum cell width is $\Delta x_{\text{min}} = 10.9$ pc at $z = 6$ and that Δx_{min} is co-moving, i.e. the cell width scales directly with the cosmological expansion factor a and therefore the physical resolution degrades with decreasing redshift, doubling, for example, over the redshift interval $z = 11 - 5$ (or $a = 0.083 - 0.167$).

To study the convergence of escape fractions with resolution, we use a 10 cMpc wide simulation, identical to SPHINX¹⁰ except with one level lower maximum refinement, i.e. the physical width of the highest resolution cells it at all times double that of SPHINX¹⁰. We show in Fig. 19 the evolution of the intrinsic LyC emissivity and global escape fraction in SPHINX¹⁰ and its lower resolution counterpart. The intrinsic LyC emissivity is very similar between the two runs before $z = 6$ but is somewhat enhanced in the lower-resolution run after that. We note (though not shown) that the UV luminosity function is very well converged in the two runs and matches well the observational constraints at the redshifts considered in Fig. 3, i.e. $z = 5, 6, 7, 8, 9, 10$. However, the global escape fraction, best compared via the 100-Myr average $f_{\text{esc},100}$, is systematically lower with lower resolution by a fixed 1–2 percentage points (actual difference, i.e. not relative). Due to the lower escape fraction, and the star formation rate being largely unaffected by resolution, as indicated by the thin solid lines in Fig. 19 showing the intrinsic rate of LyC produc-

tion per volume, the low-resolution simulation reionizes slower than SPHINX¹⁰ and is not fully reionized by the end of the run at $z \approx 5$. This is somewhat expected and a similar trend of decreasing f_{esc} with decreasing resolution has already been reported in the simulations of Ma et al. (2020). We compare in detail the correlations of f_{esc} with halo properties for the fiducial and lower resolution in Appendix C. To summarise, we find that all correlations we have studied between f_{esc} and halo properties hold, with the lower-resolution f_{esc} normalisation more or less flatly scaled down, except that that f_{esc} tends to be somewhat more suppressed with lower resolution in galaxies with low and intermediate sSFRs than in the galaxies with the highest sSFRs.

This non-convergence of f_{esc} with resolution, combined with the good convergence we find in terms of star formation, indicates that higher-resolution counterpart simulations would likely reionize too early due to their high escape fractions, even too early compared to observational constraints. However, changing the resolution seems to have similar effects on escape fractions as varying the SED model for stellar LyC luminosities within quite reasonable limits (e.g. reducing slightly the impact of binary stars), and therefore these two factors are somewhat degenerate. And we do find that changing either leaves our conclusions fairly intact on the correlation of f_{esc} with halo properties and how halos with different properties contribute to reionization.

Since Δx_{min} varies linearly with the expansion of the Universe and f_{esc} decreases with Δx_{min} , we must also conclude that the decrease we find with redshift of the global f_{esc} must be in some part due to the redshift-degradation of resolution. To determine how much the decrease in f_{esc} is due to this, we compare with vertical bars in Fig. 19 the overall drop in yellow in the global f_{esc} in SPHINX¹⁰ from $z = 11 - 5$, during which the expansion factor, and therefore also Δx_{min} , doubles, and in green, the drop in f_{esc} by directly doubling Δx_{min} in the simulation. We find that the drop due to directly doubling Δx_{min} is about 20 percent of the overall drop in f_{esc} with redshift over the Δx_{min} -doubling time. The effect of the redshift-degrading resolution is therefore sub-dominant but non-negligible, and we maintain our conclusion that the drop in f_{esc} is predominantly dictated by an overall decrease in sSFR with redshift. We finally note that the global sSFR and its decrease with redshift is well converged with resolution, as shown in Fig. 20.

5 CONCLUSIONS

We use the SPHINX suite of high redshift cosmological radiation-hydrodynamics simulations to predict the escape of ionizing LyC radiation from galaxies in the epoch of reionization. We focus our analysis on our largest 20 cMpc wide SPHINX²⁰ volume which finishes reionizing late, or at $z = 4.64$ but complement our analysis with a 10 cMpc wide volume using a slightly more luminous SED model which leads to an early reionization, finishing at $z = 6.5$. We find that our simulations agree well with the observed UV luminosity function for redshifts 5 – 10, implying that the intrinsic volume-emissivity of LyC photons is approximately correct. The reasonable reionization histories produced in turn imply that the mean escape fraction is also sensible. Our conclusions for the escape of LyC radiation from galaxies are as follows.

- As found previously by several authors, the escape fraction, f_{esc} , fluctuates quickly and strongly over time for individual galaxies. This is due to the regulation of f_{esc} by stellar feedback and leads to a “disco” reionization, where the emission of LyC photons into the IGM is at any given time dominated by a small fraction of galaxies,

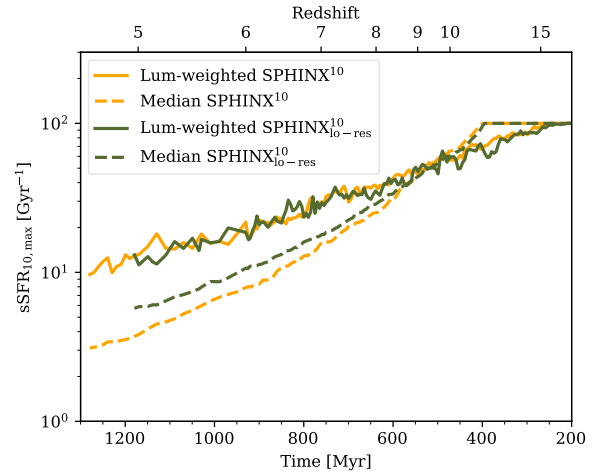


Figure 20. Redshift evolution of $\text{sSFR}_{10,\text{max}}$ in SPHINX¹⁰ and its lower-resolution counterpart. The dashed curves show the median $\text{sSFR}_{10,\text{max}}$ for all halos containing stars. Here the evolution with redshift is slightly weaker in the lower-resolution case. The solid curves show the intrinsic-LyC-luminosity-weighted mean for the same halos, showing better the evolution in $\text{sSFR}_{10,\text{max}}$ for LyC-emitting galaxies. This is barely affected by the lower resolution.

which are replaced over a few Myrs by a fresh small subset of galaxies dominating the escaping LyC emission (Fig. 7).

- The escape fraction per galaxy decreases strongly for massive halos and massive, metal-rich, bright galaxies, largely in agreement with most previous studies (Figures 8, 9, 10, and 13, respectively). We find a peak in f_{esc} for intermediate-mass galaxies of $M_* \approx 10^7 M_{\odot}$, with f_{esc} dropping strongly for both less and more massive galaxies. The same applies for brightness, with a peak at $M_{1500} \approx -17$. We find that f_{esc} correlates positively with both the short-term (Fig. 11) and long-term (Fig. 12) specific star formation rate (sSFR), through we also find high mean f_{esc} for low short-term sSFR, which we find is due to galaxies that have recently experienced high sSFR and subsequent catastrophic feedback events which caused severe disruptions of the ISM and, hence, high f_{esc}

- We find that escaping LyC radiation during the EoR comes from increasingly massive, metal-rich, and bright galaxies with decreasing redshift. This evolution is weaker though than for intrinsic emission, due to these massive, metal-rich, and bright galaxies having low escape fractions. The emission (both intrinsic and escaping) also shifts to galaxies with decreasing sSFR with redshift, due to an overall decrease in sSFR. Taking a sensitivity limit of $M_{1500} = -17$ for existing high- z surveys, we find that the bright and constrained part of the high- z luminosity function contains galaxies responsible for about 45 (52) percent of the LyC photons emitted into the IGM (produced in the ISM) up to the end of reionization (Fig. 14). The JWST, with a sensitivity limit of $M_{1500} = -16$, will account for about 68 percent of the LyC radiation contributing to reionization.

- The global f_{esc} , naturally and without any calibration, decreases with redshift in our simulations, as assumed by UV background models and low-redshift observations (Fig. 6). We find that this evolution is driven almost exclusively by a decreasing intensity of star formation (and hence feedback), measured via the maximum sSFR of a galaxy over the last 50 Myrs (Fig. 16). The current sSFR does not show as clean a correlation with f_{esc} , because a burst in star formation can lead to an increase in f_{esc} that lasts tens of Myrs after the burst has ceased and while the galaxy is effectively quenched.

- Whereas previous works have attributed the regulation of f_{esc}

primarily to SN feedback, we find that LyC radiation feedback also plays an important role (Fig. 18).

Our fiducial late reionization simulation has lower overall escape fractions and therefore a lower global escape fraction than the early reionization simulation, but otherwise the conclusions above hold for both simulations, in terms of the dependencies of f_{esc} on halo properties, the halos contributing to the LyC budget during reionization, the evolution of f_{esc} with redshift, and what drives it. Lower resolution tends to produce overall lower escape fractions, but our conclusions on the correlation of f_{esc} with halo properties and the evolution of f_{esc} with redshift hold.

ACKNOWLEDGEMENTS

We thank the referee, Nick Gnedin, for an insightful review that helped improve our manuscript. We are also grateful to JJ Eldridge and Elizabeth Stanway for help in interpreting the BPASS models. This work was supported by the National Research Foundation of Korea (NRF) grant funded by the Korea government (MSIT) (No. 2019K2A9A1A06091377 and No. 2020R1C1C1007079). Support was also provided jointly by CNRS and NRF via the “projets de recherche conjoints” (PRC) grant titled RUBGY in 2020-2021. TG acknowledges support from ERC starting grant ERC-757258-TRIPLE. LCK was supported by the European Union’s Horizon 2020 research and innovation programme under the Marie Skłodowska-Curie grant agreement No. 885990. Support by ERC Advanced Grant 320596 “The Emergence of Structure during the Epoch of reionization” is gratefully acknowledged. Computing time for this work was provided by the Partnership for Advanced Computing in Europe (PRACE) as part of the “First luminous objects and reionization with SPHINX (cont.)” (2016153539, 2018184362, 2019215124) project. We thank Philipp Otte and Filipe Guimaraes for helpful support throughout the project and for the extra storage they provided us. We also thank GENCI for providing additional computing resources under GENCI grant A0070410560. Preparations and tests were also performed at the Common Computing Facility (CCF) of the LABEX Lyon Institute of Origins (ANR-10-LABX-0066) and PSMN (Pôle Scientifique de Modélisation Numérique) at ENS de Lyon.

DATA AVAILABILITY

The data underlying this article will be shared on reasonable request to the corresponding author.

REFERENCES

- Agertz O., et al., 2020, *MNRAS*, 491, 1656
- Alvarez M. A., Finlator K., Trenti M., 2012, *ApJ*, 759, L38
- Atek H., et al., 2015, *ApJ*, 814, 69
- Atek H., Richard J., Kneib J.-P., Schaerer D., Atek H., Richard J., Kneib J.-P., Schaerer D., 2018, *MNRAS*, 479, 5184
- Aubert D., Pichon C., Colombi S., 2004, *MNRAS Letters*, 352, 376
- Bañados E., et al., 2017, *Nature*, 553, 473
- Becker G. D., D’Aloisio A., Christenson H. M., Zhu Y., Worseck G., Bolton J. S., 2021, *MNRAS*, 508, 1853
- Behroozi P., Wechsler R. H., Hearin A. P., Conroy C., 2019, *MNRAS*, 488, 3143
- Bouwens R. J., et al., 2015, *ApJ*, 803, 34
- Bouwens R. J., Oesch P. A., Illingworth G. D., Ellis R. S., Stefanon M., 2017, *ApJ*, 843, 129
- Ceverino D., Glover S., Klessen R., Ceverino D., Glover S. C. O., Klessen R. S., 2017, *MNRAS*, 470, 2791
- Davies F. B., et al., 2018, *ApJ*, 864, 142
- Dayal P., Ferrara A., Dayal P., Ferrara A., 2019, *Proc. Int. Astron. Union*, 15, 43
- Dekel A., et al., 2009, *Nature*, 457, 451
- Eldridge J. J., Izzard R. G., Tout C. A., 2007, *MNRAS*, 384, 1109
- Faisst A. L., Faisst L. A., 2016, *ApJ*, 829, 99
- Fakhouri O., Ma C.-P., Boylan-Kolchin M., Fakhouri O., Ma C.-P., Boylan-Kolchin M., 2010, *MNRAS*, 406, 2267
- Fan X., Carilli C. L., Keating B., 2006a, *Annu. Rev. Astron. Astrophys.*, 44, 415
- Fan X., et al., 2006b, *ApJ Letters*, 132, 117
- Farcy M., Rosdahl J., Dubois Y., Blaizot J., Martin-Alvarez S., 2022, *MNRAS*, 513, 5000
- Faucher-Giguère C.-A., 2020, *MNRAS*, 493, 1614
- Federrath C., Klessen R. S., 2012, *ApJ*, 761, 156
- Ferland G. J., Korista K. T., Verner D. A., Ferguson J. W., Kingdon J. B., Verner E. M., 1998, *Publ. Astron. Soc. Pacific*, 110, 761
- Fernández R. L., et al., 2018, *A&A*, 615, A27
- Ferrara A., Loeb A., Ferrara A., Loeb A., 2012, *MNRAS*, 431, 2826
- Finkelstein S. L., et al., 2015, *ApJ*, 810, 71
- Finkelstein S. L., et al., 2019, *ApJ*, 879, 36
- Garel T., Blaizot J., Rosdahl J., Michel-Dansac L., Haehnelt M. G., Katz H., Kimm T., Verhamme A., 2021, *MNRAS*, 504, 1902
- Gnedin N. Y., 2014, *ApJ*, 793, 29
- Gnedin N. Y., Kravtsov A. V., Chen H.-W., 2008, *ApJ*, 672, 765
- Grazian A., et al., 2017, *A&A*, 602, A18
- Greig B., Mesinger A., Haiman Z., Simcoe R. A., 2017, *MNRAS*, 466, stw3351
- Greig B., Mesinger A., Bañados E., 2019, *MNRAS*, 484, 5094
- Gunn J. E., Peterson B. A., Gunn J. E., Peterson B. A., 1965, *ApJ*, 142, 1633
- Haardt F., Madau P., 2012, *ApJ*, 746, 125
- Hahn O., Abel T., 2011, *MNRAS*, 415, 2101
- Heckman T. M., 2000, *arXiv:astro-ph/0009075*
- Heckman T. M., et al., 2011, *ApJ*, 730, 5
- Hutter A., et al., 2020, *MNRAS*, 506, 215
- Iliev I. T., Mellema G., Ahn K., Shapiro P. R., Mao Y., Pen U.-L., 2013, *MNRAS*, 439, 725
- Inoue A. K., Iwata I., 2008, *MNRAS*, 387, 1681
- Inoue A. K., et al., 2018, *Publ. Astron. Soc. Japan*, 70, 55
- Ishigaki M., et al., 2017, *ApJ*, 854, 73
- Jung I., et al., 2020, *ApJ*, 904, 144
- Kannan R., Garaldi E., Smith A., Pakmor R., Springel V., Vogelsberger M., Hernquist L., 2021, *MNRAS*, 511, 4005
- Katz H., Kimm T., Sijacki D., Haehnelt M. G., 2017, *MNRAS*, 468, 4831
- Katz H., Kimm T., Haehnelt M. G., Sijacki D., Rosdahl J., Blaizot J., 2018, *MNRAS*, 483, 1029
- Katz H., et al., 2020a, *MNRAS*, 494, 2200
- Katz H., et al., 2020b, *MNRAS*, 498, 164
- Katz H., et al., 2021, *MNRAS*, 510, 5603
- Keating L. C., Weinberger L. H., Kulkarni G., Haehnelt M. G., Chardin J., Aubert D., 2020, *MNRAS*, 491, 1736
- Kennicutt R. C., Evans N. J., 2012, *ARA&A*, 50, 531
- Khaire V., Srianand R., 2018, *MNRAS*, 484, 4174
- Khaire V., Srianand R., Choudhury T. R., Gaikwad P., 2015, *MNRAS*, 457, 4051
- Kimm T., Cen R., 2014, *ApJ*, 788, 121
- Kimm T., Cen R., Devriendt J., Dubois Y., Slyz A., 2015, *MNRAS*, 451, 2900
- Kimm T., Katz H., Haehnelt M., Rosdahl J., Devriendt J., Slyz A., 2017, *MNRAS*, 652, 4826
- Kroupa P., 2001, *MNRAS Letters*, 322, 231
- Kulkarni G., Keating L. C., Haehnelt M. G., Bosman S. E. I., Puchwein E., Chardin J., Aubert D., 2019, *MNRAS Letters*, 485, L24
- Laursen P., Sommer-Larsen J., Andersen A. C., 2009, *ApJ*, 704, 1640
- Lehnert M. D., et al., 2015, *A&A*, 577, A112
- Lewis J. S. W., et al., 2020, *MNRAS*, 496, 4342
- Livermore R. C., Finkelstein S. L., Lotz J. M., 2017, *ApJ*, 835, 113

Ma X., et al., 2015, *MNRAS*, 453, 960
 Ma X., Hopkins P. F., Kasen D., Quataert E., Faucher-Giguere C.-A., Keres D., Murray N., Strom A., 2016, *MNRAS*, 459, 3614
 Ma X., et al., 2018, *MNRAS*, 478, 1694
 Ma X., Quataert E., Wetzel A., Hopkins P. F., Faucher-Giguere C.-A., Kereš D., 2020, *MNRAS*, 498, 2001
 Madau P., Haardt F., Rees M. J., 1999, *ApJ*, 514, 648
 Mason C. A., et al., 2018, *ApJ*, 856, 2
 Mason C. A., et al., 2019, *MNRAS*, 485, 3947
 Matthee J., et al., 2016, *MNRAS*, 465, 3637
 Matthee J., et al., 2021, *MNRAS*
 Mauerhofer V., Verhamme A., Blaizot J., Garel T., Kimm T., Michel-Dansac L., Rosdahl J., 2021, *A&A*, 646, A80
 McGreer I., Mesinger A., D’Odorico V., 2015, *MNRAS*, 447, 499
 Meštrić U., et al., 2021, *MNRAS*, 508, 4443
 Michel-Dansac L., et al., 2020, *A&A*, 635, A154
 Naidu R. P., et al., 2019, *ApJ*, 892, 109
 Ocvirk P., et al., 2018, *MNRAS*, 496, 4087
 Ocvirk P., et al., 2021, *MNRAS*, 507, 6108
 Oesch P. A., Bouwens R. J., Illingworth G. D., Labbé I., Stefanon M., 2018, *ApJ*, 855, 105
 Ouchi M., et al., 2009, *ApJ*, 706, 1136
 Ouchi M., et al., 2017, *Publ. Astron. Soc. Japan*, 70, S13
 Paardekooper J.-P., Khochfar S., Vecchia C. D., 2015, *MNRAS*, 451, 2544
 Pahl A. J., et al., 2021, *MNRAS*, 505, 2447
 Penzias A. A., Wilson R. W., 1965, *Astrophys. J. Lett.* v.489, 142, 419
 Planck Collaboration 2014, *A&A*, 571, A1
 Planck Collaboration P., et al., 2018, *A&A*, 641, A6
 Price L. C., Trac H., Cen R., 2016, arXiv:1605.03970
 Puchwein E., Haardt F., Haehnelt M. G., Madau P., Puchwein E., Haardt F., Haehnelt M. G., Madau P., 2019, *MNRAS*, 485, 47
 Rasera Y., Teyssier R., 2006, *A&A*, 445, 1
 Razoumov A. O., Sommer-Larsen J., 2010, *Astrophys. J. Lett.* v.489, 710, 1239
 Read J. I., Iorio G., Agertz O., Fraternali F., 2017, *MNRAS*, 467, 2019
 Robertson B. E., 2021, eprint arXiv:2110.13160
 Rosdahl J., Teyssier R., 2015, *MNRAS*, 449, 4380
 Rosdahl J., Blaizot J., Aubert D., Stranex T., Teyssier R., 2013, *MNRAS*, 436, 2188
 Rosdahl J., et al., 2018, *MNRAS*, 479, 994
 Rosen A., Bregman J. N., 1995, *ApJ*, 440, 634
 Rutkowski M. J., et al., 2017, *ApJL*, 841, L27
 Saxena A., et al., 2021, *MNRAS*, 511, 120
 Schroeder J., Mesinger A., Haiman Z., 2012, *MNRAS*, 428, 3058
 Sharma M., Theuns T., Frenk C., Bower R. G., Crain R. A., Schaller M., Schaye J., 2017, *MNRAS*, 468, 2176
 Smith M. L., Bryan G. L., Somerville R. S., Hu C.-Y., Teyssier R., Burkhardt B., Hernquist L., 2020, *MNRAS*, 506, 3882
 Stanway E. R., Eldridge J. J., 2018, *MNRAS*, 479, 75
 Stanway E. R., Eldridge J. J., Becker G. D., 2016, *MNRAS*, 456, 485
 Stefanon M., Bouwens R. J., Labbé I., Illingworth G. D., Gonzalez V., Oesch P. A., 2021a, *ApJ*, 922, 29
 Stefanon M., et al., 2021b, *ApJ*, 927, 48
 Steidel C. C., et al., 2018, *ApJ*, 869, 123
 Sun G., Furlanetto S. R., 2015, *MNRAS*, 460, 417
 Tacchella S., Bose S., Conroy C., Eisenstein D. J., Johnson B. D., 2018, *ApJ*, 868, 92
 Teyssier R., 2002, *A&A*, 385, 337
 Tillson H., Miller L., Devriendt J., 2011, *MNRAS*, 417, 666
 Trebitsch M., Blaizot J., Rosdahl J., Devriendt J., Slyz A., 2017, *MNRAS*, 470, 224
 Trebitsch M., et al., 2021, *A&A*, 653, 154
 Tweed D., Devriendt J., Blaizot J., Colombi S., Slyz A., 2009, *A&A*, 506, 647
 Wise J. H., Cen R., 2009, *ApJ Letters*, 693, 984
 Wise J. H., Demchenko V. G., Halicek M. T., Norman M. L., Turk M. J., Abel T., Smith B. D., 2014, *MNRAS*, 442, 2560
 Xu H., Wise J. H., Norman M. L., Ahn K., O’Shea B. W., 2016, *ApJ*, 833, 84

Yajima H., Choi J.-H., Nagamine K., 2011, *MNRAS*, 412, 411
 Yajima H., et al., 2020, *MNRAS*, 509, 4037
 Yoo T., Kimm T., Rosdahl J., 2020, *MNRAS*, 499, 5175
 Yung L. Y. A., Somerville R. S., Finkelstein S. L., Popping G., Davé R., Venkatesan A., Behroozi P., Ferguson H. C., 2020, *MNRAS*, 496, 4574
 Zaroubi S., Zaroubi Saleem 2012, *ASSL*, 396, 45

APPENDIX A: ESCAPE FRACTIONS FOR FIXED MASSES, METALLICITIES, AND SSFR

To follow up on the discussion in §3.7 on how the evolution of the global f_{esc} with redshift is driven by an evolution in $\text{sSFR}_{10, \text{max}}$ we show here how it is not driven by an evolution in galaxy mass, metallicity, or sSFR_{10} . This is already quite clear from the redshift evolution of escape fractions in Figures 8–12 but we show it here for completeness.

We show in Fig. A1 how the escape fraction evolves for different bins in sSFR_{10} (whereas we used $\text{sSFR}_{10, \text{max}}$ in Fig. A1 in the main text). For the highest two bins, i.e. with $\text{sSFR}_{10} \geq 25 \text{ Gyr}^{-1}$, and ignoring the noise in $f_{\text{esc}, 100}$ due to small numbers of halos in these ranges, the escape fraction does remain fairly constant with redshift, and there is a significant difference of $f_{\text{esc}, 100} \approx 0.06$ for the highest sSFR_{10} bin and $f_{\text{esc}, 100} \approx 0.035$ for the second-highest bin. Also, with decreasing redshift, the total LyC luminosity goes from being dominated by high to lower sSFR_{10} halos, as indicated by the shaded regions. However, for halos with $\text{sSFR}_{10} < 25 \text{ Gyr}^{-1}$, which start to dominate the LyC emissivity below a redshift of about 8, the escape fraction does not stay constant with redshift for a fixed sSFR_{10} , but rather decreases in more or less the same way as the global escape fraction in black. A similar plot for the longer-timescale sSFR_{100} (not shown) shows an even more variability in $f_{\text{esc}, 100}$ with redshift for fixed sSFR_{100} -bins. Therefore, as we argue in the main text, $\text{sSFR}_{10, \text{max}}$ is a much better measure of the intensity of star formation and feedback than sSFR_{10} or sSFR_{100} , as it keeps memory of recent starbursts.

We then show a similar analysis in Fig. A2 for fixed galaxy mass and metallicity. The blue solid curve shows $f_{\text{esc}, 100}$ as a function of redshift for all halos in the stellar mass range $3 \times 10^6 M_{\odot} < M_{*} < 3 \times 10^7 M_{\odot}$. The dashed blue curve shows the relative contribution of those same halos to the total intrinsic LyC emissivity. The escape fraction decreases with redshift for this fixed mass-range, similarly to the the global one for all halos (solid black curve), though the global one is always lower owing to the “peak” in f_{esc} for the selected mass range in Fig. 9. The similar slope of the blue and black curves demonstrates that the decreasing escape fraction with redshift is *not* regulated by an evolution towards more massive galaxies – rather it suggests that the mass-evolution has very little effect on driving the evolution of the global escape fraction. Similarly, the red solid curve shows $f_{\text{esc}, 100}$ for halos with luminosity-weighted stellar metallicities in the range $10^{-4} < Z_{\text{halo}} < 4 \times 10^{-4}$. For this fixed metallicity range, we also see a decrease in $f_{\text{esc}, 100}$ with redshift. Although the drop is significant, it is not as strong as for fixed galaxy mass, suggesting that metallicity plays a somewhat stronger role than galaxy mass in driving a decreasing f_{esc} with redshift, though clearly it is not the dominant driver. The solid green curve finally shows $f_{\text{esc}, 100}$ for halos fixed to both the mass and metallicity ranges noted above. Once again we retrieve an escape fraction that evolves very strongly with redshift. This means that evolving galaxy masses or metallicities are not the dominant factors driving a decreasing escape fraction with redshift, neither alone nor together. We note that we have played extensively with varying the fixed ranges in both galaxy mass and metallicity and

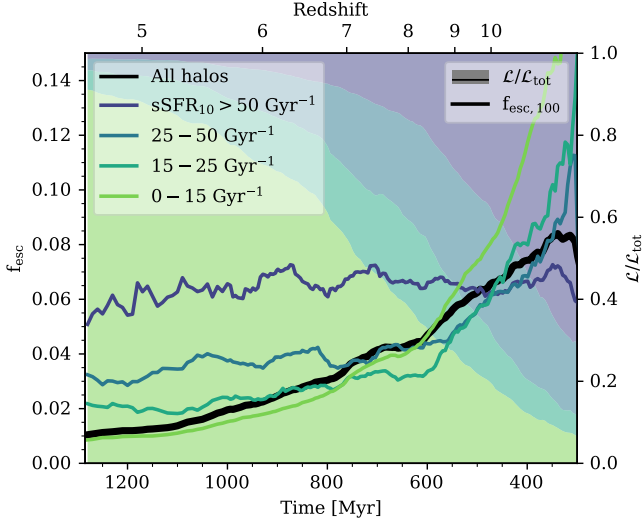


Figure A1. Global escape fraction averaged over 100 Myrs ($f_{\text{esc},100}$) versus redshift, in solid curves, for all halos in SPHINX²⁰ and for bins of fixed sSFR_{10} , as indicated in the legend. The shaded regions indicate the fractions of LyC photons intrinsically produced in these fixed sSFR_{10} bins, and show that the LyC production is dominated by decreasing sSFR_{10} with decreasing redshift. For the higher end of sSFR_{10} , halos with fixed sSFR_{10} have fairly constant mean escape fractions, but at the lower end the escape fraction still decreases with redshift for fixed sSFR_{10} , indicating some but not quite dominant redshift-regulation of f_{esc} via sSFR_{10} .

we always find a similar evolution of decreasing f_{esc} with redshift, so we are confident that neither galaxy mass nor metallicity is a major factor in regulating the f_{esc} evolution in SPHINX.

We note that a different conclusion was reached by Yoo et al. (2020), studying f_{esc} from idealised disc galaxies simulated with the same code as SPHINX and similar methods. They found metallicity to be a much stronger regulator of f_{esc} than both mass and sSFR , in conflict with our results. However, we argue that i) the galaxies in Yoo et al. (2020) are likely more relevant to galaxies with well defined disks than the messy and bursty high- z galaxies found in the EoR and ii) the sSFR ($\approx 0.1 - 1 \text{ Gyr}^{-1}$) was not tested at extreme enough values in Yoo et al. (2020) to reach the regime where f_{esc} becomes high in SPHINX.

APPENDIX B: VOLUME SIZE AND SED VARIATIONS

We collect here for reference a comparison of our main results for the different SPHINX runs, i.e. the fiducial SPHINX²⁰ run reported on in the main text, the smaller-volume but otherwise identical SPHINX¹⁰ run and the smaller-volume and more luminous SED SPHINX^{early} run. We remind the reader that due to their smaller volumes, the results from SPHINX¹⁰ and SPHINX^{early} are much noisier than those from SPHINX²⁰.

We first compare in Figures B1-B7 the dependence of f_{esc} on halo mass, galaxy mass, metallicity, sSFR_{10} , sSFR_{100} , M_{1500} , and $\text{sSFR}_{10,\text{max}}$. Here we have made sure to use only the subset of snapshots that exist in all runs, i.e. the same number of snapshots and at the same redshifts, so not as to introduce any bias in the comparison.

First focusing on volume size, for mass, metallicity, and magnitude, the escape fraction is generally slightly higher in the smaller-volume SPHINX¹⁰ run than in SPHINX²⁰, especially at the higher redshifts.

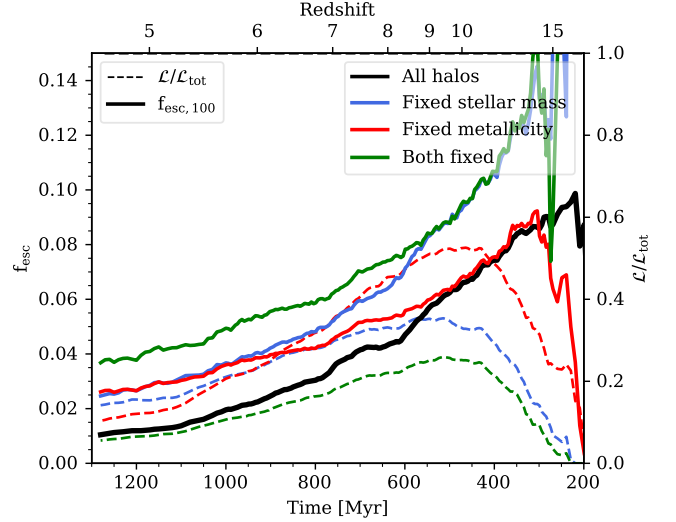


Figure A2. Global escape fractions in SPHINX²⁰ averaged over 100 Myrs ($f_{\text{esc},100}$), in solid, for all halos and at fixed halo mass ($3 \times 10^6 - 3 \times 10^7 M_{\odot}$) and/or halo (luminosity-weighted stellar) metallicity ($Z_{\text{halo}} = 10^{-4} - 4 \times 10^{-4}$), as indicated in the legend. The dashed curves show the fractions of the total number of LyC photons intrinsically produced by halos in these fixed mass and metallicity ranges. Fixing either halo mass or metallicity gives consistently larger $f_{\text{esc},100}$ than in the unfiltered case, simply due to the chosen ranges corresponding to high escape fractions. Fixing the metallicity reduces the redshift-evolution of $f_{\text{esc},100}$ somewhat more than fixing the halo mass, indicating that evolving metallicity has a stronger regulating effect on the escape fraction than halo mass. However, even for fixed metallicity the escape fraction is far from non-evolving with redshift, so halo mass and metallicity, alone or together, do not regulate the decrease of global escape fraction with redshift.

We are not sure why but speculate that this hints at a small but non-negligible environmental effect on f_{esc} , i.e. galaxies of a given mass and metallicity residing in massive environments tend to have lower escape fractions. We will explore this in future work. The larger difference between the volume sizes is that the intrinsic LyC emission is shifted towards significantly more massive and metal-rich halos. Because these halos have small f_{esc} , this translates to a much smaller difference in the *escaping* emission, shown in purple curves. For sSFR_{10} and $\text{sSFR}_{10,\text{max}}$, the intrinsic LyC emission is shifted to higher sSFR s in SPHINX¹⁰ compared to SPHINX²⁰ and f_{esc} is noticeably higher in SPHINX¹⁰ at intermediate sSFR_{10} . Both are effects of the relative lack of massive galaxies with are luminous but have low escape fractions. This difference is sort of smoothed out for the longer-term sSFR_{100} , where f_{esc} is just overall slightly higher for SPHINX¹⁰.

Then focusing on the different SED models and comparing SPHINX¹⁰ and SPHINX^{early}, the more luminous SED model leads to f_{esc} being overall higher in SPHINX^{early} for any halo property correlation considered, i.e. the correlation as a whole shifts to higher f_{esc} , due to more LyC photons being emitted at ages of $\gtrsim 5$ Myrs in the more luminous model (see Figures 1 and 18). The cumulative intrinsic LyC fraction tends to be very similar for the two models and mostly this is also the case for the *escaping* emission.

To summarise, there is no significant or surprising difference in the dependence of f_{esc} on halo properties when changing the volume size or SED model, except for an unexplained slight overall increase

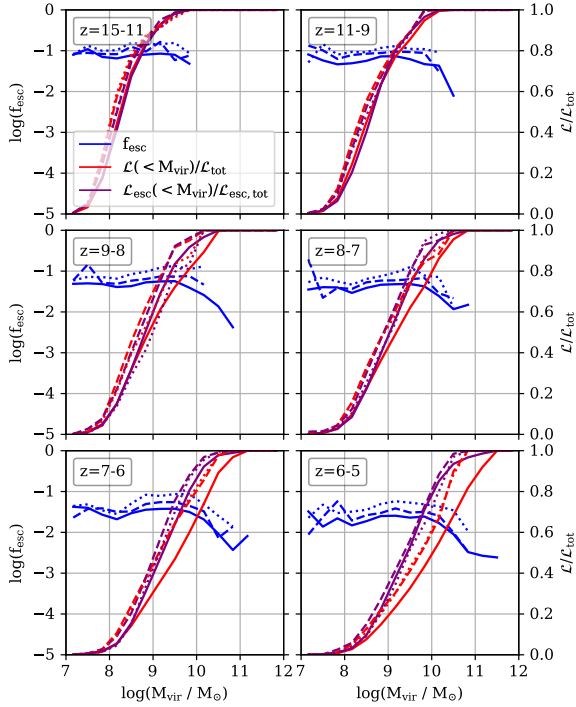


Figure B1. f_{esc} versus M_{vir} correlation, cumulative intrinsic emissivity, and cumulative escaping LyC emissivity (blue, red, and purple curves, respectively) at different redshifts, same as Fig. 8 but here compared for SPHINX²⁰, the smaller volume SPHINX¹⁰, and the smaller volume plus more luminous SED SPHINX¹⁰_{early} simulations (solid, dashed, and dotted curves, respectively).

The smaller volume case shows a hint of higher f_{esc} than in SPHINX²⁰, especially at the highest redshifts. The more luminous SED increases f_{esc} even further and roughly equally for any halo mass. Intrinsic luminosities vary significantly between the two volume sizes but escaping luminosities much less so due to the low f_{esc} of massive halos.

in f_{esc} with a smaller volume, which we speculate may be due to environmental effects.

We show in Figures B8 and B9 the contributions to emitted and escaping LyC radiation of halos of different properties in the smaller-volume SPHINX¹⁰ run and luminous SED SPHINX¹⁰_{early} run, respectively. Qualitatively they are in both cases similar to SPHINX²⁰. Keep in mind, again, that the data is significantly more noisy than in SPHINX²⁰, especially at high redshift. Due to the smaller volume, the intrinsic contribution in SPHINX¹⁰ is shifted a somewhat towards objects that are less massive, less metal-rich, and dimmer. However, due to the low escape fractions of the massive, bright, and metal-rich galaxies that are “missing” in SPHINX¹⁰, the shift is much smaller for escaping LyC contributions. The effect of the more luminous SED model in SPHINX¹⁰_{early} is to shift contributions slightly back to higher masses, metallicities, and brighter galaxies, compared to SPHINX¹⁰, if taking the total contribution to the LyC budget at $z \approx 5$. However, if we consider the contribution at the end of reionization and factor in that reionization finishes at $z = 5.1$ in SPHINX¹⁰ but a dex and a half earlier in SPHINX¹⁰_{early}, the contributions shift back again and become fairly similar between the two simulations. Hence we conclude that the contributions of halos to reionization are very similar between the three simulations considered and for all the halo properties considered.

We finally demonstrate that the evolution of the global escape fraction in the SPHINX²⁰ simulation is driven by decreasing $\text{sSFR}_{10,\text{max}}$,

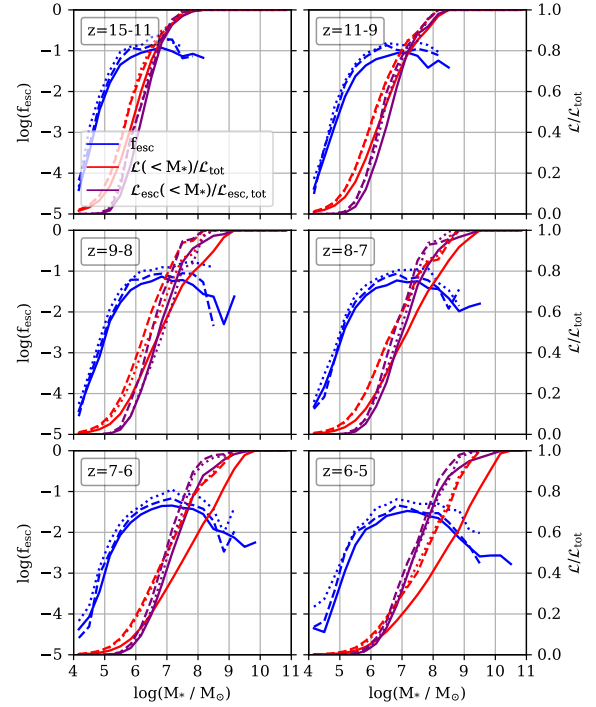


Figure B2. As Fig. B1 but for galaxy mass M_* . The smaller volume shows higher f_{esc} than in SPHINX²⁰ at high- z . The more luminous SED increases f_{esc} overall, i.e. at any galaxy mass. Intrinsic luminosities vary significantly between the two volume sizes but escaping luminosities much less so due to the low f_{esc} of massive galaxies.

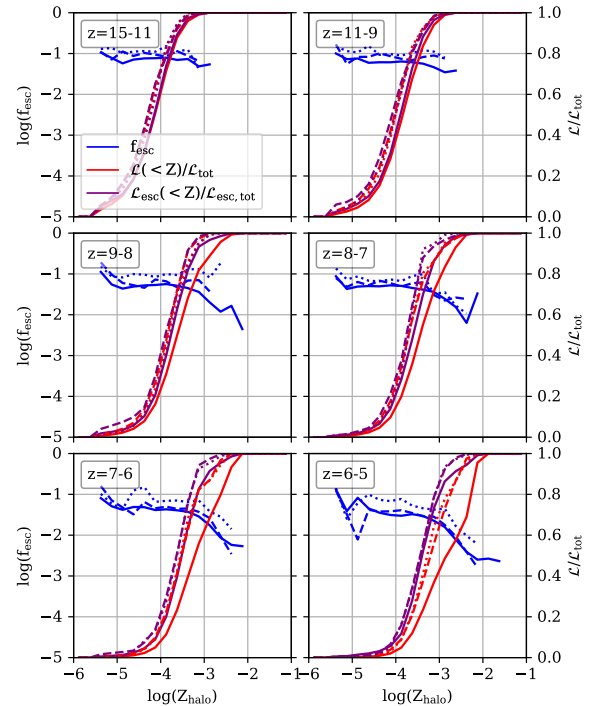


Figure B3. As Fig. B1 but for galaxy metallicity. The smaller volume shows higher f_{esc} than in SPHINX²⁰ at high- z . The more luminous SED increases f_{esc} overall, i.e. at any metallicity. Intrinsic luminosities vary significantly between the two volume sizes but escaping luminosities much less so due to the low f_{esc} of metal-rich galaxies.

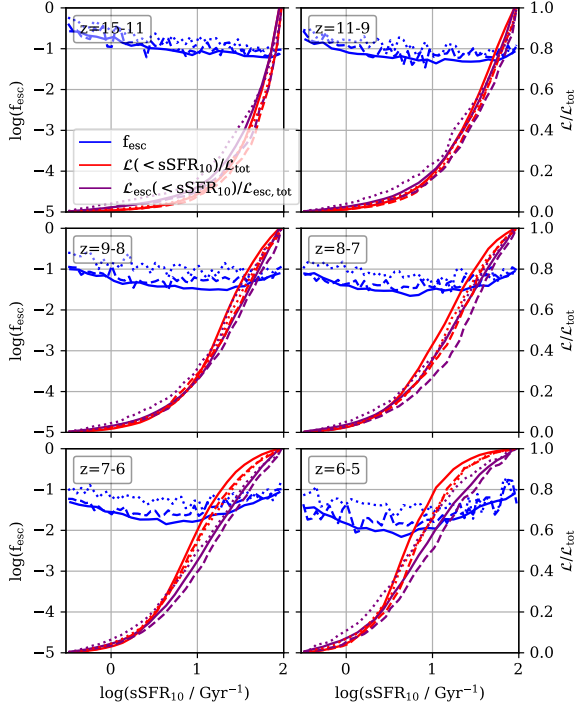


Figure B4. As Fig. B1 but for $sSFR_{10}$. The smaller volume shows higher f_{esc} than in SPHINX²⁰ for intermediate $sSFR_{10}$, likely due to the galaxies being less massive. The more luminous SED increases f_{esc} overall but least significantly at the highest $sSFR_{10}$. Here escaping luminosities vary somewhat between the runs, especially at the lowest- z , with the escaping luminosity notably shifted to moderate $sSFR_{10}$ in the case of the more luminous SED model.

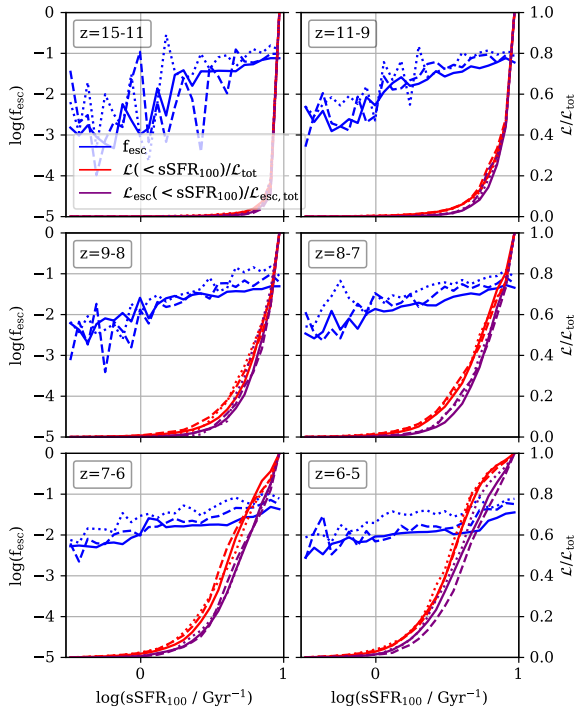


Figure B5. As Fig. B1 but for $sSFR_{100}$. The luminous SED increases f_{esc} overall, but there is small difference in intrinsic or escaping emissivities.

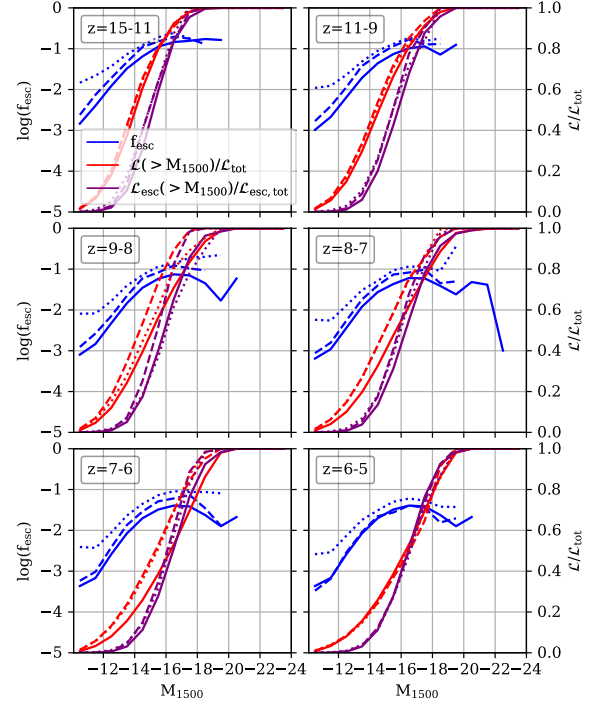


Figure B6. As Fig. B1 but for M_{1500} . The smaller volume has higher f_{esc} than SPHINX²⁰ at high- z . The luminous SED increases f_{esc} overall, but there is small difference in intrinsic or escaping.

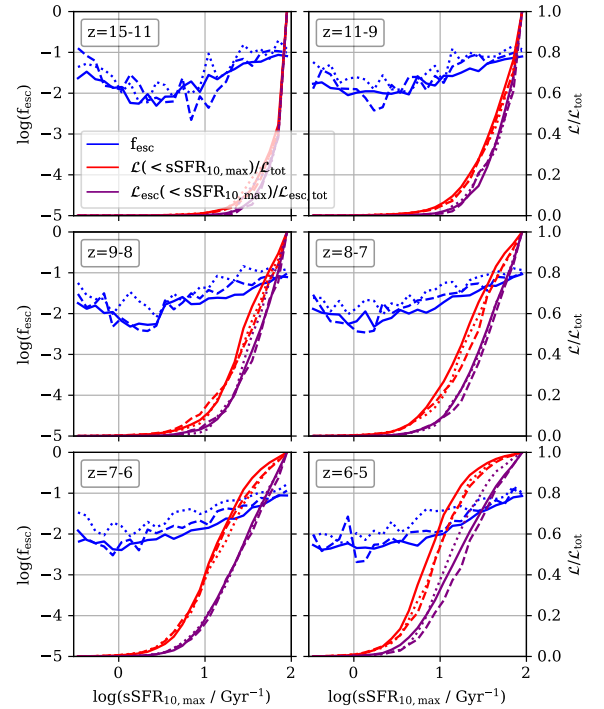


Figure B7. As Fig. B1 but for $sSFR_{10,\text{max}}$. The data is noisy for the small-volume simulations, especially at low $sSFR_{10,\text{max}}$. The more luminous SED increases f_{esc} overall. For all runs, the $f_{\text{esc}}-sSFR_{10,\text{max}}$ relation is fairly non-evolving with redshift (except for low $sSFR_{10,\text{max}}$ where little LyC radiation is emitted anyway), implying that the evolving global f_{esc} is driven by the shift to lower $sSFR_{10,\text{max}}$ in the smaller volumes, just as in SPHINX²⁰.

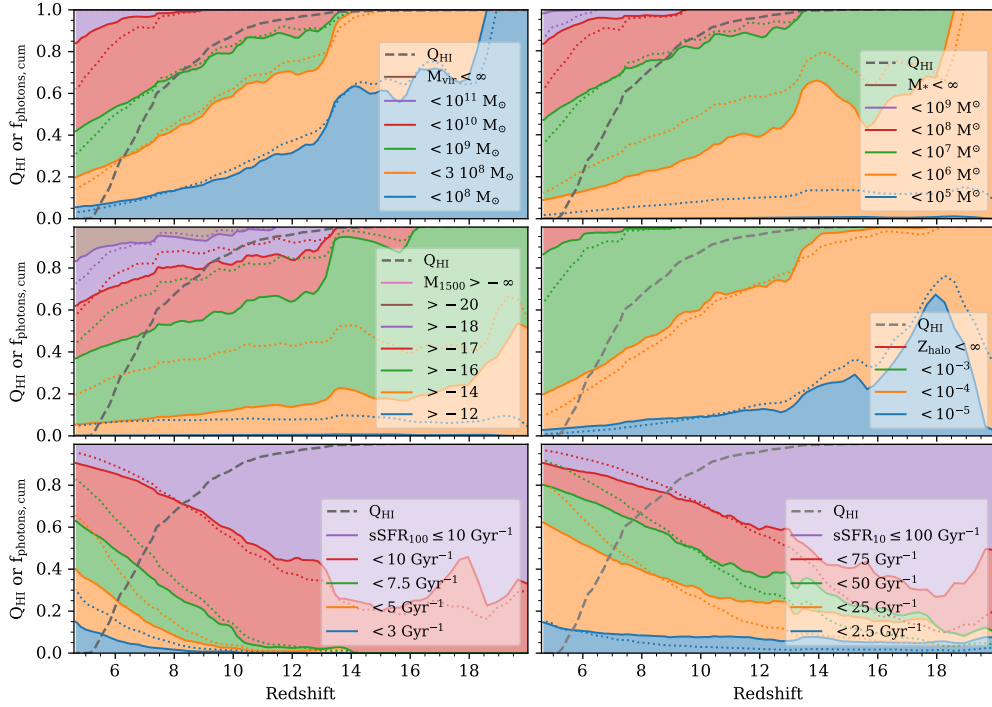


Figure B8. Contributions of different halos to reionization in the 10 cMpc SPHINX¹⁰ volume (with BPASS v2.2.1). Compared to the larger-volume but otherwise identical SPHINX²⁰ run (Fig. 14), the intrinsic LyC emission (dotted curves) is shifted to lower masses, lower metallicities, and dimmer magnitudes. However, since the ‘extra’ massive, metal-rich and bright galaxies represented in SPHINX²⁰ but not in SPHINX¹⁰ tend to have low escape fractions, the escaping luminosities are significantly less shifted. For sSFRs, both the intrinsic and escaping emission is very similar between SPHINX¹⁰ and SPHINX²⁰.

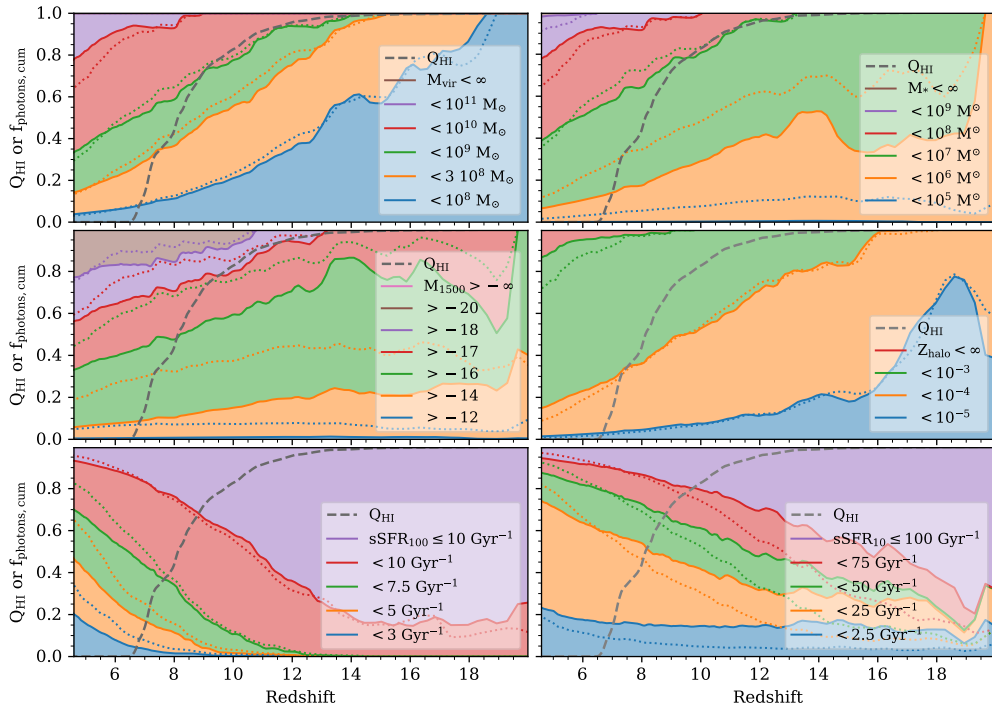


Figure B9. Contributions of different halos to reionization in the 10 cMpc SPHINX^{10_early} volume (with BPASS v2.0). Compared to SPHINX¹⁰ (Fig. B8), which is identical save for the SED version, both intrinsic and escaping contributions to the LyC budget by $z = 5$ are shifted somewhat to more massive, brighter, more metal-rich, and less star-forming galaxies. However, taking into account that reionization finishes ≈ 1.5 dex earlier in SPHINX^{10_early}, halo contributions by the end of reionization ($z = 5.1$ in SPHINX¹⁰, $z = 6.5$ in SPHINX^{10_early}) are actually for the most part shifted very slightly in the opposite direction.

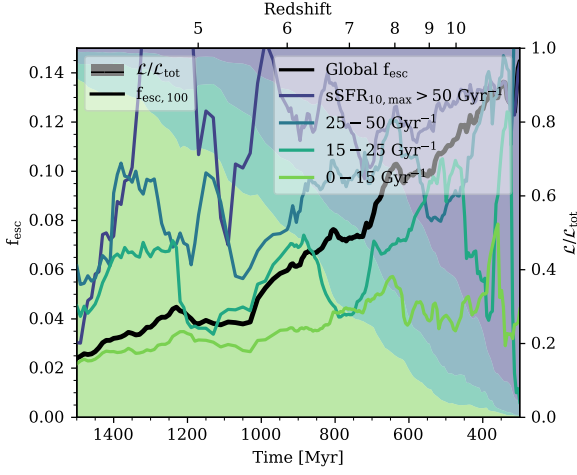


Figure B10. Global escape fractions in the SPHINX¹⁰ run averaged over 100 Myrs ($f_{\text{esc},100}$) versus redshift, in solid, for all halos and at fixed bins in $\text{sSFR}_{10,\text{max}}$, as indicated in the legend. The shaded regions indicate the fractions of the total LyC radiation intrinsically produced by halos in these fixed $\text{sSFR}_{10,\text{max}}$ bins. This is the same as Fig. 16 but for a smaller volume and the more LyC-luminous SED model. The data is much noisier than in Fig. 16 (due to the small volume), but we still find a clear difference in f_{esc} between the $\text{sSFR}_{10,\text{max}}$ -bins and the global evolution in f_{esc} still appears driven mostly by this difference and the evolution in $\text{sSFR}_{10,\text{max}}$.

just as it is in SPHINX²⁰. We show in Fig. B10 a dissection of the evolving global escape fraction in SPHINX¹⁰ for halos with different $\text{sSFR}_{10,\text{max}}$, just like in Fig. 16 for SPHINX²⁰. Once again there is much more noise in the data for this smaller volume simulation, especially for halo categories that contain relatively few halos. Despite large fluctuations it is still fairly clear that the decrease with redshift in the global f_{esc} is largely driven by an evolution where the LyC radiation is emitted from halos with decreasing $\text{sSFR}_{10,\text{max}}$ and hence decreasing f_{esc} . Our conclusion – that the decreasing f_{esc} with redshift is driven by an increasing fraction of galaxies with low $\text{sSFR}_{10,\text{max}}$ with redshift in the expanding Universe – holds for both our simulations bracketing the observational constraints on the reionization history of the Universe.

APPENDIX C: RESOLUTION CONVERGENCE

We repeat the exercise of the previous appendix, now comparing our fiducial resolution SPHINX¹⁰ run to an identical run with one level lower maximum resolution, i.e. the minimum cell width is twice as large at any point in the simulation. The resulting correlations of f_{esc} versus halo properties are shown in Figures C1-C7 with SPHINX¹⁰ in solid curves and its lower-resolution counterpart in dashed curves. Generally the correlations of f_{esc} with the halo properties considered are unaffected, with f_{esc} being simply overall lower with lower resolution, but with a somewhat enhanced difference for the highest metallicities and intermediate-to-high sSFR_{10} and $\text{sSFR}_{10,\text{max}}$.

APPENDIX D: FITS FOR ESCAPE FRACTIONS

In case the escape fractions measured in SPHINX may be useful for analytic models of reionization or to compare to other simulation works, we provide here our fits for the correlations of f_{esc} with the

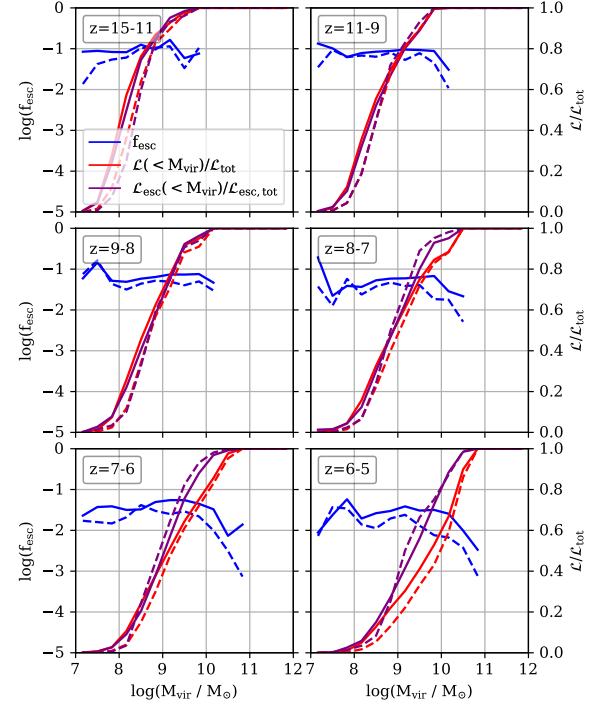


Figure C1. Correlation of f_{esc} with M_{vir} , cumulative intrinsic emissivity, and cumulative escaping LyC emissivity (blue, red, and purple curves, respectively) at different redshifts, same as Fig. 8 but here compared for SPHINX¹⁰, in solid curves, and an identical lower resolution run with double the minimum cell width at any point, shown in dashed curves.

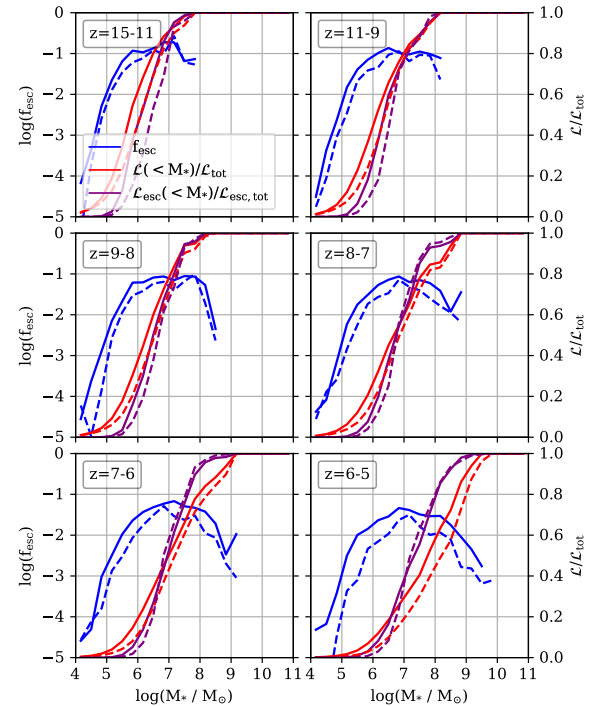


Figure C2. As Fig. C1 but for f_{esc} versus galaxy mass M_* .

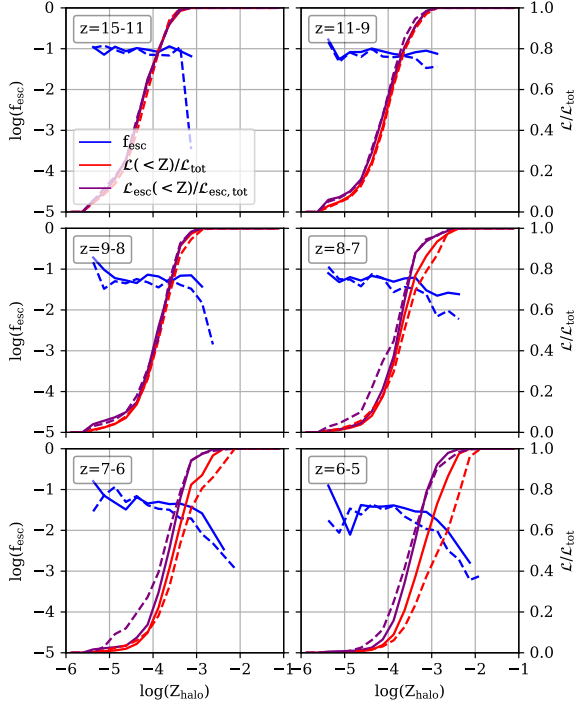


Figure C3. As Fig. C1 but for f_{esc} versus galaxy metallicity.

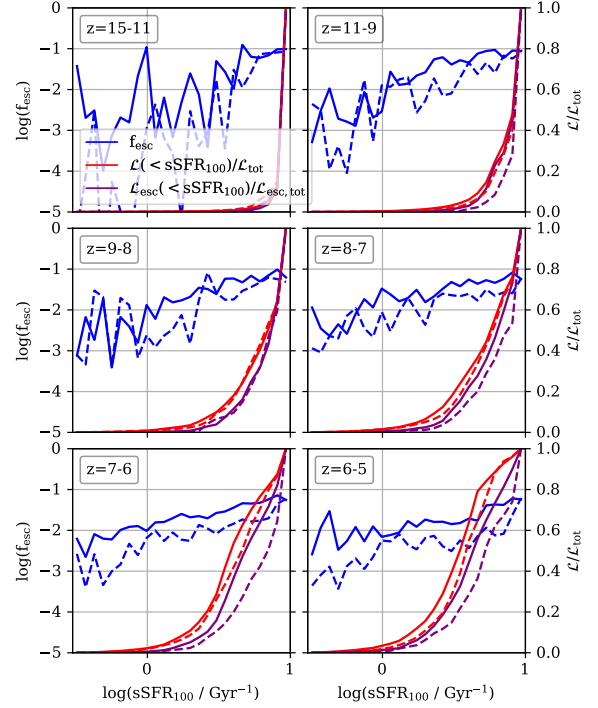


Figure C5. As Fig. C1 but for f_{esc} versus $s\text{SFR}_{100}$.

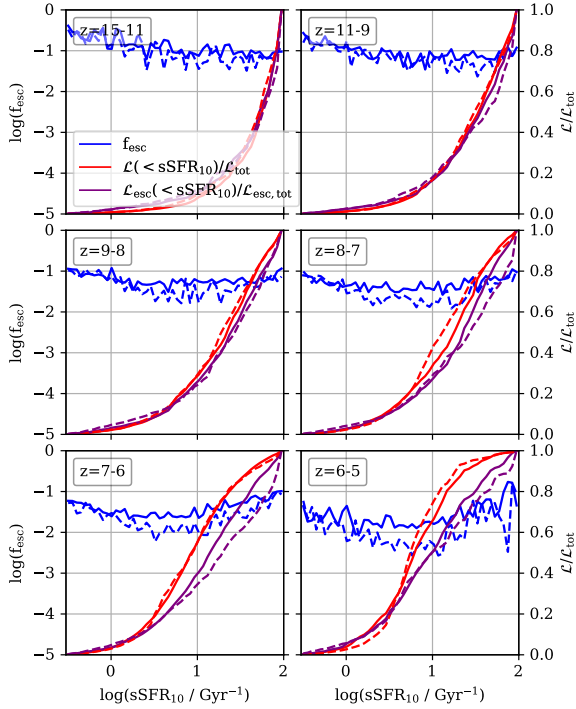


Figure C4. As Fig. C1 but for f_{esc} versus $s\text{SFR}_{10}$.

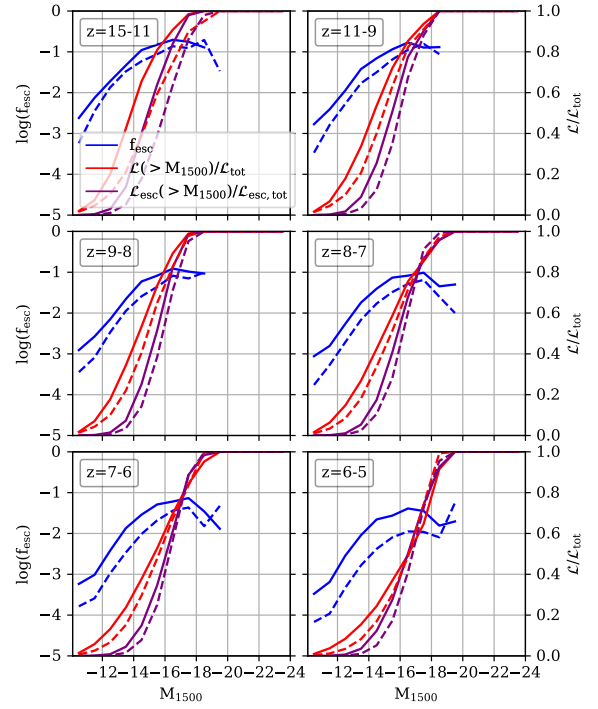


Figure C6. As Fig. C1 but for f_{esc} versus M_{1500} .

various halo properties plotted in Figures 8 - 13 and Fig. 15. The fits are shown in each of those figures in transparent blue curves. The fitted function is in all cases the logarithm of a third degree polynomial, i.e.

$$f_{\text{esc}}(x) = 10^{a+bx+cx^2+dx^3}, \quad (\text{D1})$$

where x is (typically the base-10 logarithm of) the halo property under consideration. We use the `scipy.optimize.curve_fit` fitting function to derive the best-fit values for the polynomial coefficients a, b, c, d for each halo property and at each redshift range considered. We use the default parameters for the `curve_fit` function, i.e. we use the “least squares” fitting method, we do not provide any guess

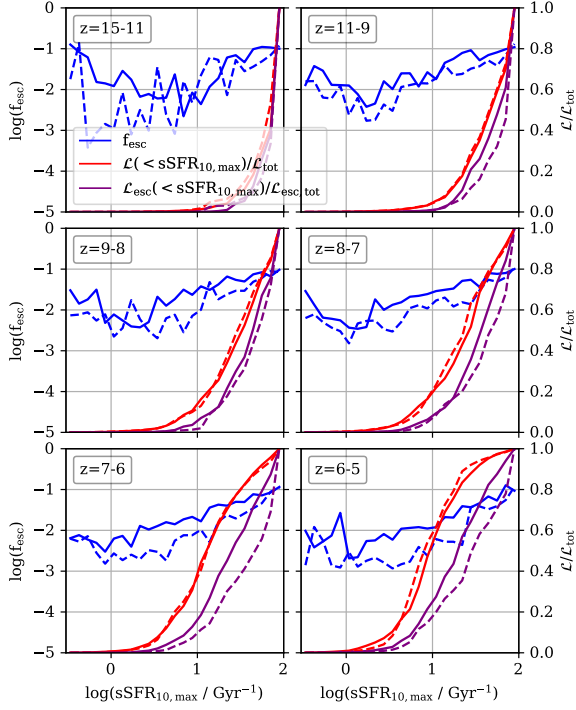


Figure C7. As Fig. C1 but for f_{esc} versus $\text{sSFR}_{10,\text{max}}$.

for the best fit, we do not weigh by uncertainties, and we do not assume any bounds. We do, however, exclude any f_{esc} data from the simulations represented by less than 100 halos. This is why the fits sometimes cover a shorter range than the histograms in Figures 8 - 13 and Fig. 15.

We provide the best-fit values for the polynomial coefficients a, b, c, d in Table D1, which also includes the ranges for which our fits are valid.

This paper has been typeset from a $\text{\TeX}/\text{\LaTeX}$ file prepared by the author.

Table D1. Our polynomial coefficient fits for the correlation of f_{esc} with the halo properties considered in this paper at various redshift ranges, using the third-degree polynomial $f_{\text{esc}}(x) = 10^{a+bx+cx^2+dx^3}$. The first row gives the name of the halo property which goes into the polynomial as the x parameter. The second column gives the relevant redshift range. The third column gives the range in the halo property x for which the fit is valid, and the last four columns give the best fit coefficients.

Halo property x	redshift range	x-range	a	b	c	d
$\log(M_{\text{vir}}/M_{\odot})$	$z = 15 - 11$	$\log(M_{\text{vir}}/M_{\odot}) = [7, 9.7]$	5.3570	-1.9448	0.1874	-0.0057
	$z = 11 - 9$	$\log(M_{\text{vir}}/M_{\odot}) = [7, 10]$	104.5197	-37.6354	4.4391	-0.1735
	$z = 9 - 8$	$\log(M_{\text{vir}}/M_{\odot}) = [7, 10.3]$	54.3631	-19.9959	2.3789	-0.0938
	$z = 8 - 7$	$\log(M_{\text{vir}}/M_{\odot}) = [7, 10.7]$	60.6799	-22.3502	2.6610	-0.1048
	$z = 7 - 6$	$\log(M_{\text{vir}}/M_{\odot}) = [7, 11]$	77.7443	-27.8650	3.2448	-0.1252
	$z = 6 - 4.7$	$\log(M_{\text{vir}}/M_{\odot}) = [7, 11.7]$	24.4699	-9.2316	1.0853	-0.0425
$\log(M_*/M_{\odot})$	$z = 15 - 11$	$\log(M_*/M_{\odot}) = [4, 7.7]$	-53.4495	22.1841	-3.0984	0.1428
	$z = 11 - 9$	$\log(M_*/M_{\odot}) = [4, 8.3]$	-39.8329	15.2711	-1.9774	0.0838
	$z = 9 - 8$	$\log(M_*/M_{\odot}) = [4, 8.7]$	-35.3369	12.9054	-1.5841	0.0626
	$z = 8 - 7$	$\log(M_*/M_{\odot}) = [4, 9]$	-28.2177	9.4517	-1.0492	0.0358
	$z = 7 - 6$	$\log(M_*/M_{\odot}) = [4, 9.3]$	-27.5989	9.0776	-0.9955	0.0335
	$z = 6 - 4.7$	$\log(M_*/M_{\odot}) = [4, 10.3]$	-27.2628	9.0356	-1.0212	0.0364
$\log(Z_{\text{halo}})$	$z = 15 - 11$	$\log(Z_{\text{halo}}) = [-5.3, -3]$	-18.2132	-12.3055	-2.9206	-0.2284
	$z = 11 - 9$	$\log(Z_{\text{halo}}) = [-5.3, -2.7]$	-10.5256	-6.7514	-1.6252	-0.1300
	$z = 9 - 8$	$\log(Z_{\text{halo}}) = [-5.3, -2.7]$	-20.9345	-14.4295	-3.4955	-0.2793
	$z = 8 - 7$	$\log(Z_{\text{halo}}) = [-5.3, -2.3]$	-13.1098	-8.5654	-2.0575	-0.1635
	$z = 7 - 6$	$\log(Z_{\text{halo}}) = [-5.3, -2]$	-7.5847	-4.0109	-0.8745	-0.0649
	$z = 6 - 4.7$	$\log(Z_{\text{halo}}) = [-5.3, -1.7]$	-7.8124	-4.1390	-0.9282	-0.0722
$\log(\text{sSFR}_{10}/\text{Gyr}^{-1})$	$z = 15 - 11$	$\log(\text{sSFR}_{10}/\text{Gyr}^{-1}) = [-0.45, 2]$	-0.7918	-0.4428	0.1651	-0.0200
	$z = 11 - 9$	$\log(\text{sSFR}_{10}/\text{Gyr}^{-1}) = [-0.45, 2]$	-1.0398	-0.4359	0.1510	0.0218
	$z = 9 - 8$	$\log(\text{sSFR}_{10}/\text{Gyr}^{-1}) = [-0.45, 2]$	-1.2243	-0.4452	0.0820	0.0914
	$z = 8 - 7$	$\log(\text{sSFR}_{10}/\text{Gyr}^{-1}) = [-0.45, 2]$	-1.3863	-0.4905	0.2776	0.0252
	$z = 7 - 6$	$\log(\text{sSFR}_{10}/\text{Gyr}^{-1}) = [-0.45, 2]$	-1.5840	-0.5096	0.3093	0.0504
	$z = 6 - 4.7$	$\log(\text{sSFR}_{10}/\text{Gyr}^{-1}) = [-0.45, 2]$	-1.9525	-0.6187	0.8167	-0.1412
$\log(\text{sSFR}_{100}/\text{Gyr}^{-1})$	$z = 15 - 11$	$\log(\text{sSFR}_{100}/\text{Gyr}^{-1}) = [-0.45, 2]$	-2.4597	1.9507	0.8506	-1.5870
	$z = 11 - 9$	$\log(\text{sSFR}_{100}/\text{Gyr}^{-1}) = [-0.5, 1]$	-2.2077	1.5319	0.7636	-1.4199
	$z = 9 - 8$	$\log(\text{sSFR}_{100}/\text{Gyr}^{-1}) = [-0.5, 1]$	-1.8990	1.0351	-0.2655	-0.2329
	$z = 8 - 7$	$\log(\text{sSFR}_{100}/\text{Gyr}^{-1}) = [-0.5, 1]$	-1.9739	0.8402	-0.4007	0.2843
	$z = 7 - 6$	$\log(\text{sSFR}_{100}/\text{Gyr}^{-1}) = [-0.5, 1]$	-1.9435	0.5844	-0.4538	0.4819
	$z = 6 - 4.7$	$\log(\text{sSFR}_{100}/\text{Gyr}^{-1}) = [-0.5, 1]$	-2.0670	0.2429	-0.6316	1.1331
M_{1500}	$z = 15 - 11$	$M_{1500} = [-10.5, -17.5]$	-5.2932	0.3721	0.0902	0.0031
	$z = 11 - 9$	$M_{1500} = [-10.5, -18.5]$	3.0704	2.2120	0.2186	0.0060
	$z = 9 - 8$	$M_{1500} = [-10.5, -18.5]$	5.0293	2.6969	0.2557	0.0070
	$z = 8 - 7$	$M_{1500} = [-10.5, -19.5]$	-1.6847	1.2212	0.1476	0.0044
	$z = 7 - 6$	$M_{1500} = [-10.5, -19.5]$	-1.5486	1.3384	0.1596	0.0047
	$z = 6 - 4.7$	$M_{1500} = [-10.5, -20.5]$	-10.3763	-0.4500	0.0386	0.0020
$\log(\text{sSFR}_{10,\text{max}}/\text{Gyr}^{-1})$	$z = 15 - 11$	$\log(\text{sSFR}_{10,\text{max}}/\text{Gyr}^{-1}) = [-0.45, 2]$	-2.0148	-0.6498	1.2940	-0.3616
	$z = 11 - 9$	$\log(\text{sSFR}_{10,\text{max}}/\text{Gyr}^{-1}) = [-0.45, 2]$	-1.9890	-0.2057	0.7240	-0.1960
	$z = 9 - 8$	$\log(\text{sSFR}_{10,\text{max}}/\text{Gyr}^{-1}) = [-0.45, 2]$	-2.0879	-0.2526	0.9023	-0.2701
	$z = 8 - 7$	$\log(\text{sSFR}_{10,\text{max}}/\text{Gyr}^{-1}) = [-0.45, 2]$	-2.1417	-0.1700	0.7125	-0.1745
	$z = 7 - 6$	$\log(\text{sSFR}_{10,\text{max}}/\text{Gyr}^{-1}) = [-0.45, 2]$	-2.2493	-0.1025	0.6510	-0.1438
	$z = 6 - 4.7$	$\log(\text{sSFR}_{10,\text{max}}/\text{Gyr}^{-1}) = [-0.45, 2]$	-2.4119	-0.0168	0.5724	-0.1002